Dielectric characterization and polarimetric analysis of lunar north polar crater Hermite-A using Chandrayaan-1 Mini-SAR, Lunar Reconnaissance Orbiter (LRO) Mini-RF, and Chandrayaan-2 DFSAR data

Awinash Singh [a,b], Aanchal Sharma [a], Shashi Kumar [a,*], Ling Chang [b], Ankita Vashishtha [a], Rahul Raj [c], Shefali Agrawal [a], Prakash Chauhan [d]

[a] *Indian Institute of Remote Sensing (IIRS), Indian Space Research Organisation (ISRO), 04 Kalidas Road, Dehradun 248001, Uttarakhand, India*
[b] *Faculty of Geo-Information Science and Earth Observation (ITC), University of Twente, Enschede 7514 AE, The Netherlands*
[c] *Institute of Bio- and Geosciences: Agrosphere (IBG-3), Forschungszentrum Jülich GmbH, Jülich 52428, Germany*
[d] *National Remote Sensing Centre (NRSC), Hyderabad 500037, Telangana, India*

Abstract

Studies of the lunar surface from Synthetic Aperture Radar (SAR) data have played a prominent role in the exploration of the lunar surface in recent times. This study uses data from SAR sensors from three Moon missions: Chandrayaan-1 Mini-SAR, Lunar Reconnaissance Orbiter (LRO) Mini-RF and Chandrayaan-2 Dual Frequency Synthetic Aperture Radar (DFSAR). DFSAR sensor is the first of its kind to operate at L-band and S-band in fully and hybrid polarimetric modes. Due to the availability of only L-band data out of the two bands (L-and S-band) for the study site, this study only used DFSAR's L-band data. The dielectric characterization and polarimetric analysis of the lunar north polar crater Hermite-A was performed in this study using Chandrayaan-1 Mini-SAR, LRO Mini-RF and Chandrayaan-2 DFSAR data. Hermite-A lies in the Permanently Shadowed Region (PSR) of the lunar north pole and whose PSR ID is NP_879520_3076780. Because of its location within the PSR of the lunar north pole, the Hermite-A makes an ideal candidate for a probable location of water-ice deposits. This work utilizes S-band hybrid polarimetric data of Mini-SAR and Mini-RF and L-band fully polarimetric data of DFSAR for the lunar north polar crater Hermite-A. This study characterizes the scattering mechanisms from three decomposition techniques of Hybrid Polarimetry namely m-delta, m-chi, and m-alpha decompositions, and for fully polarimetric data Barnes decomposition technique was applied which is based on wave dichotomy. Eigenvector and Eigenvalue-based decomposition model (H-A-Alpha decomposition) was also applied to characterize the scattering behavior of the crater. This study utilizes the hybrid-pol and fully polarimetric data-based Integral Equation Model (IEM) to retrieve the values of dielectric constant for Hermite-A crater. The dielectric constant values for the Hermite-A crater from Chandrayaan-1 Mini-SAR and LRO Mini-RF are similar, which goes further in establishing the presence of water-ice in the region. The values of the dielectric constant for Chandrayaan-2 in some regions of the crater especially on the left side of the crater is also around 3 but overall the range is relatively higher than the compact/hybrid polarimetric data. The dielectric characterization and polarimetric analysis of the Hermite-A indicatively illustrate that the crater may have surface ice clusters in its walls and on some areas of the crater floor, which can be explored in the future from the synergistic use of remote sensing data and in-situ experiments to confirm the presence of the surface ice clusters.

* Corresponding author.
E-mail addresses: singh-3@student.utwente.nl (A. Singh), aanchalsharma7333@gmail.com (A. Sharma), shashi@iirs.gov.in, sksinghiirs@gmail.com (S. Kumar), ling.chang@utwente.nl (L. Chang), ankitavashishtha@gmail.com (A. Vashishtha), r.raj@fz-juelich.de (R. Raj), shefali_a@iirs.gov.in (S. Agrawal), prakash@iirs.gov.in (P. Chauhan).

1. Introduction

The moon, Luna (In Latin) the most fascinating and nearest celestial body which is the brightest and largest as seen in the clear night sky and the earth's only natural satellite whose distance is approximately 384,400 km from earth, the only place outside our planet where human beings have reached and explored the surface. Exploration of the lunar surface is quite interesting and profound to us in a lot of ways, but a question always arises to some of us, why the moon is important to us? The answer to this is thoroughly instructive as the moon is believed to be formed around 4.5 billion years ago when a mars size object, Theia hit the earth's surface and this event caused the birth of our Moon in this vast solar system (Herwartz et al., 2014). The moon's importance played a major role in its existence as it controlled the spin axis of the earth from its gravity, at that time the earth's spin was much faster in comparison to the present day which was around 5 h (Crawford, 2015). It is also believed that the moon and earth once shared the same magnetic field and must have lost it completely by 1.5 billion years ago (Landau, 2020). The existence and its evolution played a vital role in the existence of our planet as a large celestial body revolving around our planet made the orbit of the earth stable. Another role is of tidal effects that reduced the spin of the earth from 5 h to around 24 h as earlier our planet was spinning too fast. The most important is the lunar tides, from where the marine life from the seas came into existence which in this case is the result of the origination of the life of the land, too (Crawford, 2015).

The moon is also a source of most of the mineralogical resources which can be used for future space missions as a good product of substitute of fuels that can be used for future deep space explorations and the colonization of mankind on the lunar surface (Bhandari & Srivastava, 2014). The recent findings of water ice content on its poles which is believed to be buried or mixed with the regolith and the water ice content findings apart from the poles also show good hope in achieving our goals in near future and inching towards our desire for deep space exploration (Hayne et al., 2021; Li et al., 2018; Spudis et al., 2013). The dependence on the extraction of minerals and the economic activity related to it has been limited to one planet. The use of lunar resources can be used for the exploration of the lunar surface and they can also be used for the scientific and economic activity of both earth and moon as well as for the exploration of the other celestial bodies in the solar system. Recent studies talk about the potential resources on the lunar surface mainly solar wind implanted volatiles, Helium-3, water, oxygen, metals (platinum group metals), Iron and siderophile elements, titanium, aluminium, silicon, rare earth elements, thorium, and uranium (Bhandari & Srivastava, 2014). The continued exploration of the lunar surface will give a positive result in our goals that can be achieved soon.

The continuous missions to the moon in the 21st century by several space agencies such as SELENE (commonly known as KAGUYA, Japan), Chang' e-1, 2, 3, and 4 (China), Lunar Reconnaissance Orbiter (LRO, USA), and Chandrayaan-1 & 2 (India) gives insightful information about the lunar surface and the finding of water in its surface is a boon to several upcoming missions. In the past few decades, there is a halt in particularly manned missions to the moon and to collect the samples but the intent of 'return to the moon' and Chang' e-5 (robotic sample return mission) gives us hope to explore its surface that has been unexplored till now and more findings of water on the lunar surface will work as a catapult to several other space missions, especially Mars and maybe future deep space missions. The presence of water in large quantities on the moon could be a dominant constituent in future missions as this can be used for drinking, cooling equipment, breathing, and making rocket fuel for future space missions.

Recent studies were done by Stratospheric Observatory for Infrared Astronomy (SOFIA) and Lunar Reconnaissance Orbiter (LRO) giving an insight into the water on the sunlit moon and micro cold traps on the moon, respectively (Hayne et al., 2021; Honniball et al., 2021). Remote sensing plays a pivotal role in providing information to the earth's surface as well as the planetary surfaces. Synthetic Aperture Radar (SAR) data mainly depends on system parameters that include wavelength, polarization, and angle of incidence and target parameters that include structural and electrical properties of the targeted object (Woodhouse, 2006). It was first suggested by Arnold about the possible sources of water ice at the lunar poles (Arnold, 1979). Most of the areas of lunar poles, especially the impact craters are permanently shadowed regions that do not receive light from solar radiation because of the small inclination of 5° in the rotation (Li et al., 2018). As a result of this, the surface temperatures in this region are very low and are the probable location of water ice. These areas are called as Permanently Shadowed Region (PSR) of the moon. Dielectric characterization of the lunar surface especially the polar regions will give insightful information about the possible locations of water ice.

Several studies have been done in the past to calculate the dielectric constant values of the lunar regolith to identify the possible locations of water ice deposits in the regolith and this was done by various modeling techniques

(Shukla et al., 2020). By performing the Odelevsky model in one of the works done by (Meng et al., 2010) to extract the dielectric constant of the lunar regolith for the Cabeus crater. It was done with the relation of microwave brightness temperature and dielectric constant of the regolith. This was done with the data of the microwave radiometer onboard the Chang'e-1 satellite. The Campbell's inversion model (Campbell et al., 2002) was used by (Calla et al., 2014a) for analyzing the dielectric constant over hybrid polarimetric data of Mini-RF and it was developed on the relationship between measured radar backscattering and dielectric constant over Mars analogue environments on Earth. This model works when the radar measurements are made in vertical polarization and linear horizontal and for rock dust surfaces. This model uses the HH and VV polarizations for calculations of the backscattering coefficient and it also utilizes the density factor of soil as an input parameter in addition to the storage factor to calculate the loss factor. Another work was done by (Bhattacharya et al., 2015) which used a model that was proposed by them to predict the dielectric permittivity of the regolith of the lunar surface. As it is known that the hybrid polarimetry data of Mini-RF and Mini-SAR are available in Stokes parameter and under the condition of reflection symmetry, coherency matrix is extracted and it is then used to calculate the particle anisotropy parameter. The dielectric permittivity and its relationship with anisotropy are used for the estimation. The use of density and any deduced knowledge of density is not used in this model. This model also assumes that the regolith is a random cloud of small randomly oriented ellipsoidal particles. The model predicts that the shape ratio and orientation distribution of the constituent regolith particles are the factors on which the dielectric permittivity is based.

SAR data can be used to study the geophysical parameters of the lunar surface and it can be done with help of polarimetric data-based scattering properties retrieval of the lunar surface (Vashishtha & Kumar, 2021; Kumar et al., 2022a). Polarimetric SAR (PolSAR) can differentiate scattering elements in a single resolution cell (Babu et al., 2022; Garg et al., 2022; Maiti et al., 2021; Verma et al., 2022). A target area is an area that contributes to three types of scattering patterns namely Surface scattering, double-bounce scattering, and volume scattering and the mixture of these scattering patterns gives precise details about the physical properties of the target area (Kumar et al., 2019, 2020, 2022b). Temperature, mineral content, grain size, moisture, density, frequency, etc. are the factors that influence the electrical properties of a material. One of the most important electrical parameters of the lunar surface that provides basic data imperative for further exploration of the surface is the Dielectric constant, which can be calculated at microwave frequency using the scattering coefficient (Shukla, 2019; Shukla et al., 2020). The main objective of this research is to utilize compact and fully polarimetric SAR data for dielectric characterization of the Hermite-A crater and comparison with the map of ice

clusters that were generated in the previous studies for the permanently shadowed region (Li et al., 2018; Tavares, 2018).

2. Study area and data

The study area chosen in this study is the Hermite-A crater which is situated in the lunar North Pole. Hermite-A crater is located in proximity to a large crater called Hermite. The diameter of this crater is approximately around 20 km and its coordinates are 87.8° N and 47.1° W. It is also known as one of the coldest places in the solar system as its temperature is around 26 K. Most of the part of this crater is in PSR and it is also called a twin of Shackleton because of its bowl-shaped structure (Calla et al., 2016).

Permanently shadowed regions (PSRs) are often compared to cold traps, but these are not necessarily the same thing since energy re-radiated from illuminated slopes can generate regions where water ice cannot survive geologically. Williams et al. (2019) provided thermal data for the north pole and south pole from the Diviner polar temperature data, which shows 5300 km^2 of permanent cold traps (110 K maximum annual temperature) and 13,000 km^2 respectively for the north and south pole (Williams et al., 2019). Williams et al. (2019) also concluded that the seasonal cold traps are 17,500 km^2 for the north pole and 24,300 km^2 for the south (Cannon et al., 2020; Williams et al., 2019). Li et al. (2018) concluded that around 3.5% of cold traps exhibit ice exposures. It has been demonstrated with spectral modeling that some ice-bearing pixels may contain up to 30 wt% ice mixed with dry regolith. The observation of spectral features of H_2O shows that water ice is trapped and accumulates on the Moon in regions that are permanently shadowed, and that in some locales, it is exposed at the surface of the Moon's modern optical atmosphere (Li et al., 2018). There are deposits in the permanently shaded craters near the south pole consistent with a thick ferroan anorthosite regolith containing 1670 ± 890 ppm hydrogen, which would equal to 1.5 ± 0.8% weight fraction of H_2O. There is also a possibility of 1.35×10^8 (2.4×10^8) metric tons of water ice within the area of 2250 (4000) km^2 areas estimated to be in permanent shade in the south and 0.62×10^8 metric tons of water ice within the 1030 km^2 of estimated shade in the north (Feldman et al., 2000, 2001). Previously it was estimated that the lunar cold traps occupy around 10^4 km^2 then a ten-meter-thick pure subsurface ice deposit in all cold traps could account for up to 100 billion tons of water ice on the Moon (Paige et al., 2010; Rubanenko et al., 2019). Both of the polar regions cover a large amount of PSR and are considered to be very cold (Fisher et al., 2017; Spudis et al., 2013; Vasavada et al., 1999).

This study utilizes the datasets of three lunar missions Chandrayaan-1 (ISRO-India), LRO (NASA-USA), and Chandrayaan-2 (ISRO-India), and the SAR sensors used

in this mission are Mini-SAR, Mini-RF, and DFSAR respectively. Chandrayaan-1's mission of the Indian Space research Organisation (ISRO) took place in 2008 and consisted of several payloads which included Mini-SAR as well. The major scientific objective of this instrument was to detect water ice in the PSRs on the lunar poles up to a depth of a few meters (Bhandari & Srivastava, 2014). Mini-SAR used S-band and has a wavelength of 12.6 cm and has incidence angle of 35°. The spatial resolution of the image strips is 75 m per pixel and the mode of acquisition is monostatic (Spudis et al., 2009). Preliminary results that were concluded from Mini-SAR were that the CPR values in the North Polar Regions were in the range of 0.1–0.3. A group of craters was identified that showed a high CPR value between 0.6 and 1.7 in the interior of the crater, but it was less on the exterior of the rim of the crater, which was around 0.2–0.4. The LRO was launched in 2009 and a developed version of the SAR instrument of the Chandrayaan-1 mission was on board i.e., Mini-RF. Mini-RF instrument has a hybrid polarimetry architecture and is a side-looking radar operating in circular transmit and linear receive mode in S-band and X-band. The antenna beamwidth is 4.8° in azimuth and 8.5° in elevation and it is available in monostatic and bistatic modes. Initially, it operated in the monostatic mode but after the failure of the transmitter Arecibo Observatory in Puerto Rico was used as a transmitter at the S-band wavelength. It focuses on the lunar poles that were unexplored earlier for the possible locations of ice deposits, volatile, impact, and volcanic processes on the moon. It has also mapped the PSR of the lunar poles for the polar volatiles (Vondrak et al., 2010). The DFSAR instrument aboard Chandrayaan-2 is a dual-frequency monostatic system operating at the L-band (24 cm) and S-band (12 cm) at an altitude of 100 km. One of the main features of this radar sensor is that it is the first L-band polarimetric SAR that is utilized for lunar studies, which will be used for deeper penetration into the regolith and it is also the first fully polarimetric SAR to orbit the moon. The instrument can also acquire imaging in single, dual, and hybrid-circular polarimetry and the resolution capacities from 2 m to 75 m in the slant range with incidence angles ranging from 9.6° to 36.9° (Patterson et al., 2020; Putrevu et al., 2020). The fully polarimetric mode in this aims for unambiguous detection and the characterization and quantitative estimation of the water-ice in the permanently shadowed region of the lunar poles. Table 1 provides information on LRO Mini-RF data and Chandrayaan-1 Mini-

Table 1
Dataset details of Hybrid Polarimetry data used.

Sr No.	Sensor Name	Scene-Id	Band
1	LRO Mini-RF	lsz_06871_1cd_xku_88n304_v1	S
2	Chandrayaan-1 Mini-SAR	fsb_01744_1cd_xiu_85n339_v1	S

Table 2
Dataset detail of fully polarimetric data used.

Sr No.	Sensor Name	Date of Acquisition	Scene-Id ch2_sar_nrxl	Band
1	Chandrayaan-2 DFSAR	19-10-2019	20191019t011733461_d_fp_d18	L
2	Chandrayaan-2 DFSAR	16-11-2019	20191116t220423370_d_fp_d18	L

SAR data. Table 2 provides the information on the 2 scenes of the L-band DFSAR data that are used for polarimetric characterization and dielectric estimation of the Hermite-A crater.

Fig. 1 shows the mosaic of 60 scenes of Chandrayaan-2 DFSAR data for the north pole of the lunar surface. The details of these scenes are shown in Table A1 of Appendix A. The color composite of L-band DFSAR data is seen in this mosaic which is a Lexicographic RGB representation of level-2 Map projected, Seleno Referenced Image (SRI) data. The Clementine Basemap has been used in the background to give a proper interpretation of the lunar surface. The Clementine Basemap was downloaded from the USGS Astrogeology Science Centre (https://astrogeology.usgs.gov/). The red areas show the PSR region on the lunar surface. The PSR region of the lunar surface was taken from the Lunar Orbiter Laser Altimeter (LOLA) and it could be downloaded from the LROC website (https://lroc.sese.asu.edu/psr).

As shown in Fig. 2(a) that the Hermite-A crater is seen with the area of its PSR and its PSR ID is NP_879520_3076780 to cover the maximum area of the crater mosaic of two scenes of the SRI product were used (ch2_sar_nrxl_20191019t011733461_d_fp_d18 and 20191116t220423370_d_fp_d18). Fig. 2(b) shows the Pauli color composite of Single Look Complex (SLC) Slant range Image (SLI) data, which also shows volume scattering in the crater.

3. Methodological approach

The methodology adopted in this study for polarimetric characterization of Hermite-A crater for Mini-SAR and Mini-RF datasets is shown in Fig. 3. Five decomposition techniques have been used in this study. It includes three decomposition techniques for Hybrid-polarimetry data of LRO Mini-RF and Chandrayaan-1 Mini-SAR and two for fully polarimetric L-band data of DFSAR of Chnadrayaan-2. These are used for the characterization of the lunar crater based on the scattering patterns involved in these regions. The decomposition technique involved in this study for Hybrid polarimetry data are m-delta, m-alpha, and m-chi decomposition and for fully polarimetric data is the Barnes decomposition technique and H-A-alpha decomposition technique which is based on the polarimetric parameters.
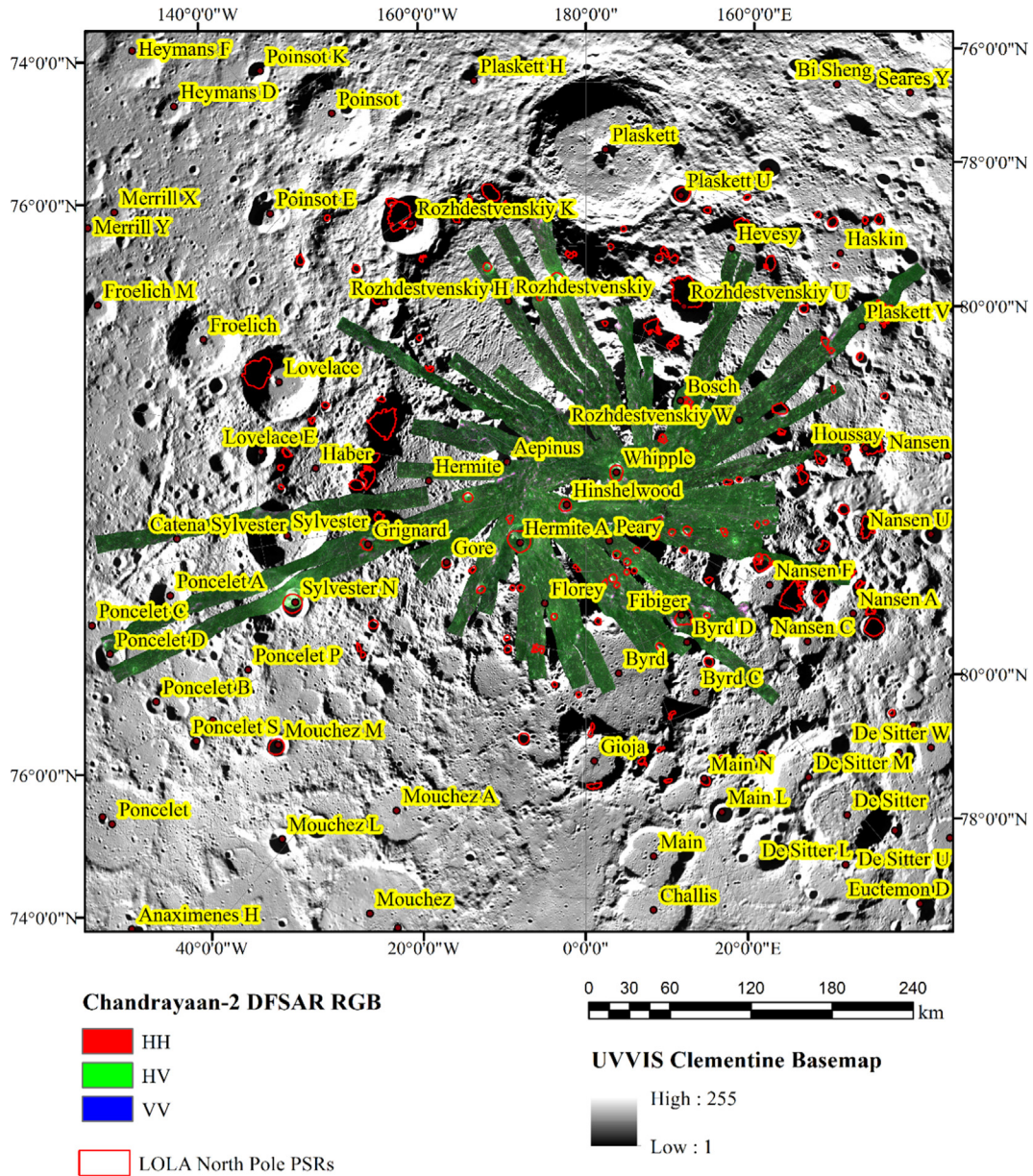
Fig. 1. Mosaic of the North Pole color composite images of the Chandrayaan-2 DFSAR scene with the names of the craters and permanently shadowed region (Red polyline). Clementine base map is used in the background to show the North Polar Region.

The data format involved in these for both LRO Mini-RF and Chandrayaan-1 Mini-SAR is a CDR dataset that consists of four bands, and each has different channels of data. The Level 1 data file of Chandrayaan-1 Mini-SAR consists of four pieces of information (Kausika, 2013; Reid, 2011).

Band 1 = Horizontal channel with configuration as $|LH|^2$

Band 2 = Vertical channel with configuration as $|LV|^2$

Band 3 = Real value of $LH \times LV^*$

Band 4 = Imaginary value of $LH \times LV^*$

There are four channels of four bytes per pixel in a strip of LRO Mini-RF and Chandrayaan-1 Mini-SAR data. Chandrayaan-1's Mini-SAR transmitted left circular polarisation and received linearly polarised horizontal and vertical components of the electric field vectors. LH represents the transmission of left circular polarisation and H and V show the receiving of linearly polarimetric horizontal and vertical polarisations. This is shown by $|LH|^2$, $|LV|^2$, real $(LH \times LV^*)$, and imaginary $(LH \times LV^*)$. Horizontally and vertically receiving intensity images are shown in $|LH|^2$ and $|LV|^2$ respectively. The real and imaginary components $(LH \times LV^*)$, respectively, represent the real and
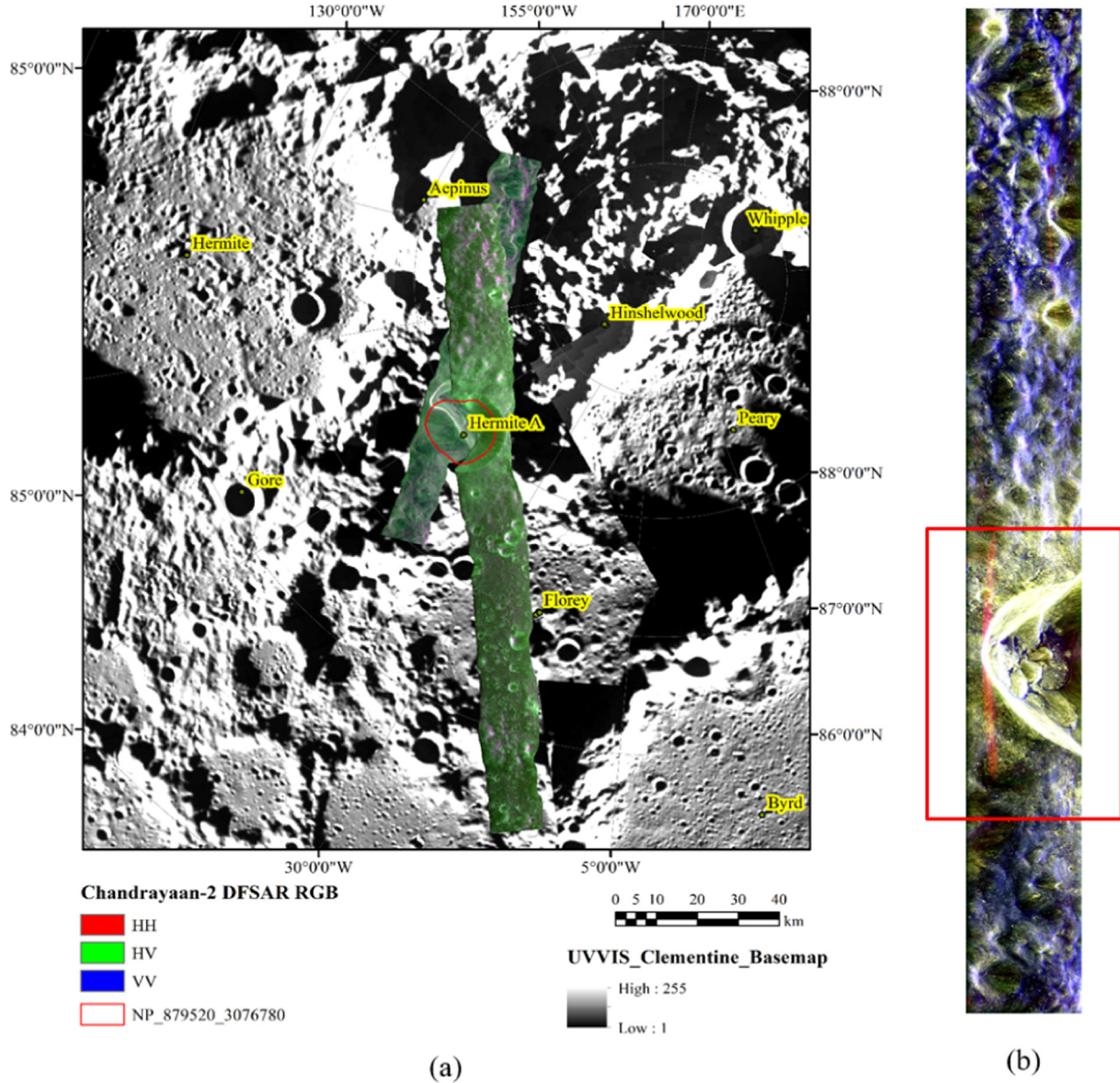
Fig. 2. (a) Lexicographic RGB presentation of level-2 Map Projected, Seleno Referenced Image (SRI) data (ID-ch2_sar_nrxl_2019101t011733461_d_fp_d18, ch2_sar_ncxl_20191116t220423370_d_fp_d18)(PSR is shown in red polyline whose PSR ID is NP_879520_3076780) (b) Pauli Color composite of Single Look Complex (SLC) Slant Range Image (SLI) data.

imaginary components of the complex value for the cross power intensity image between horizontally and vertically receiving (Calla et al., 2014a; Mohan et al., 2011). These are used to derive the four Stokes Parameters which are shown in Eq. (1). S_1, S_2, S_3, and S_4 are the four Stokes parameters.

$$\begin{Bmatrix} S_1 \\ S_2 \\ S_3 \\ S_4 \end{Bmatrix} = \begin{Bmatrix} band\ 1 + band\ 2 = <|LH|^2 + |LV|^2 > \\ band\ 1 - band\ 2 = <|LH|^2 - |LV|^2 > \\ 2 \times band\ 3 = 2\ Re < LH.LV^* > \\ (-2) \times band\ 4 = -2\ Im < LH.LV^* > \end{Bmatrix} \tag{1}$$

After the evaluation of the Stokes parameters, Stokes child parameters can be evaluated which are used in the decomposition techniques for Hybrid Polarimetry data.

So, from Stokes child parameters m, δ, and χ is calculated and the degree of polarization (m) is calculated from Eq. (2).

$$m = \frac{\sqrt{S_2^2 + S_3^2 + S_4^2}}{S_1} \tag{2}$$

The degree of polarization for a completely polarized wave is 1 and for a completely unpolarized wave is 0.

The relative phase (δ) denotes double bounce scattering and is calculated as per Eq. (3).
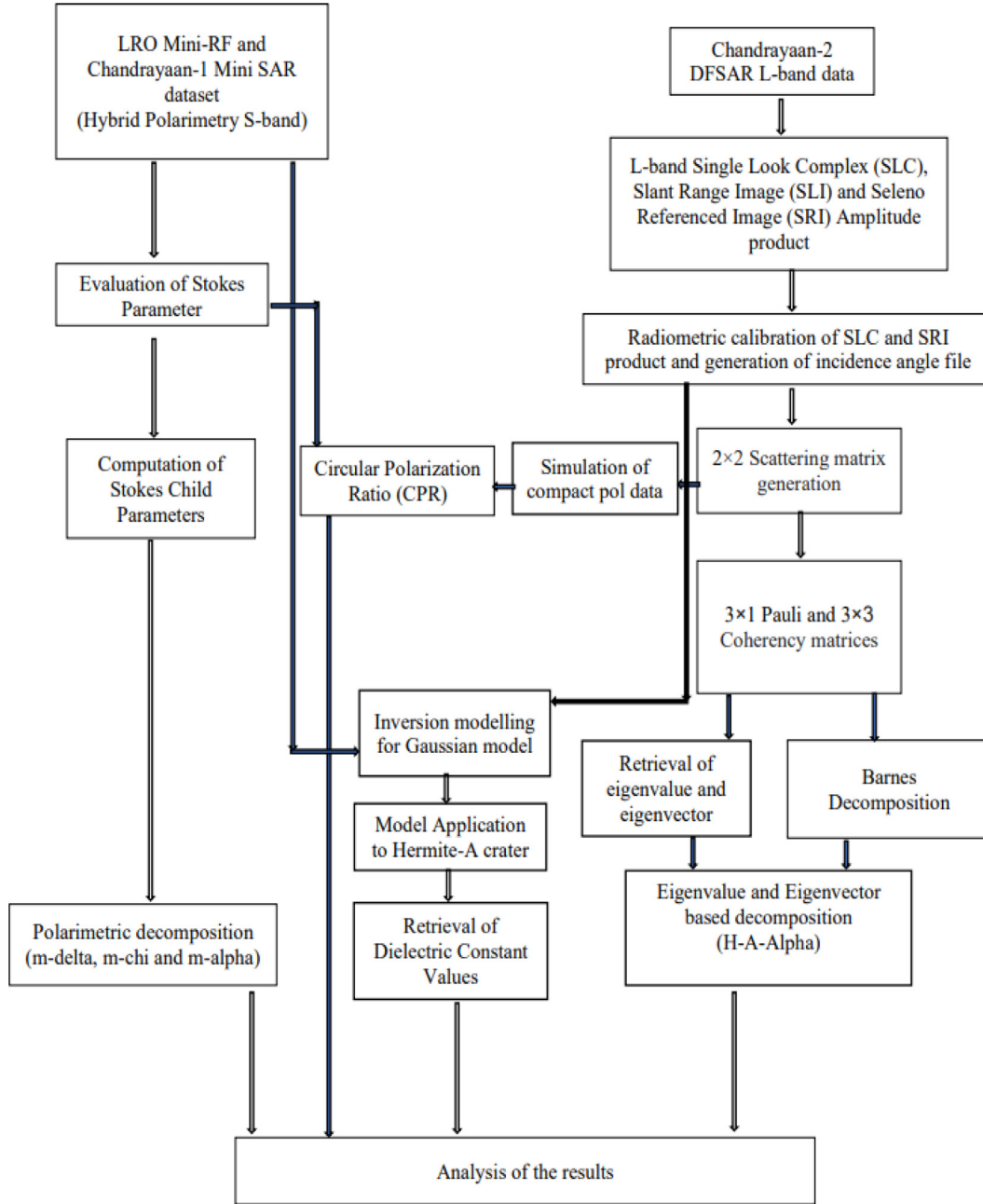
Fig. 3. Methodological Flow Diagram.

$$\delta = \tan^{-1}(s_4/s_3) \tag{3}$$

The ellipticity parameter (χ) is sensitive to double bounce scattering compared to the surface scattering and is calculated as per Eq. (4).

$$\mathrm{Sin}2\chi = -S_4/mS_1 \tag{4}$$

3.1. m-δ decomposition

This decomposition is mainly used in land and oceanic research fields to differentiate between surface and double bounce scattering. The parameters in this decomposition

are m, relative phase, and orientation angle (δ) (Raney et al., 2012). It is calculated by Eqs. (5), (6), (7).

$$s = \left[mS_1 \frac{(1 + sin\delta)}{2}\right]^{1/2} \tag{5}$$

$$v = [S_1(1 - m)]^{1/2} \tag{6}$$

$$d = \left[mS_1 \frac{(1 - sin\delta)}{2}\right]^{1/2} \tag{7}$$

Where, s = odd-bounce scattering, v = volumetric scattering, and d = even-bounce scattering.

The parameters are dependent mainly on two components δ and degree of polarization (m). δ differentiates
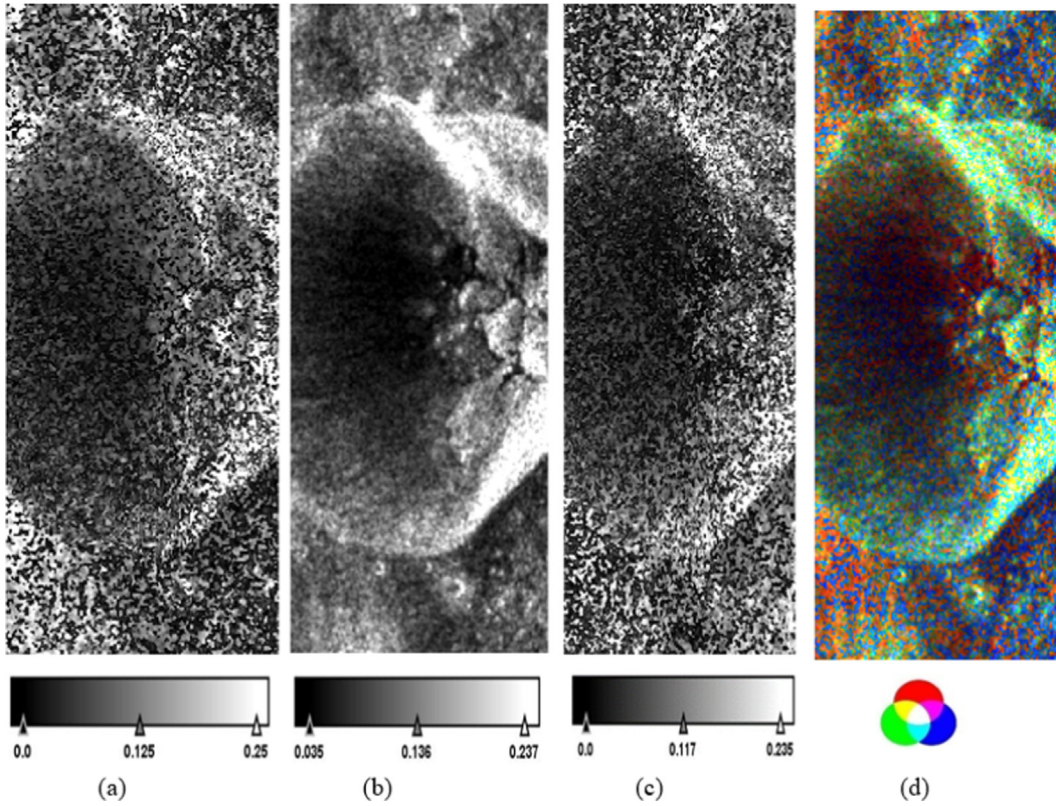
Fig. 4. m-delta decomposition of Chandrayaan-1 (Mini-SAR) (a) Double-bounce scattering, (b) Volume scattering, (c) Surface scattering, and (d) RGB color composite.

between surface and double bounce which makes it an important parameter. So, the positive value of δ shows signs of the dominance of surface scattering and the negative value for the double bounce scattering dominance.

3.2. m-χ decomposition

This decomposition is widely used in differentiating even-bounce scattering from odd-bounce scattering from the lunar surface and the parameters that are used are m, χ, and S_1. This decomposition technique was the first time used by Raney in hybrid polarimetric data (Raney et al., 2012) and was used in several other applications (Tomar et al., 2019). Calculations of the parameters in this decomposition are shown in Eqs. (8), (9), (10).

$$s = [mS_1 \frac{(1 - sin2\chi)}{2}]^{\frac{1}{2}} \tag{8}$$

$$v = [S_1(1 - m)]^{\frac{1}{2}} \tag{9}$$

$$d = [mS_1 \frac{(1 + sin2\chi)}{2}]^{\frac{1}{2}} \tag{10}$$

Where, s = odd-bounce scattering, v = volumetric scattering, and d = even-bounce scattering.

3.3. m-α decomposition

This decomposition is derived from the m-α decomposition method which is based on eigenvalue and the parameters are the degree of polarization (m) and polarization angle (α) (Tomar, 2015). α is calculated from Eq. (11).

$$\alpha = 2|\chi| \tag{11}$$

m-α decomposition is calculated by Eqs. (12), (13), (14).

$$s = [mS_1 \frac{(1 + cos2\alpha)}{2}]^{1/2} \tag{12}$$

$$v = [S_1(1 - m)]^{1/2} \tag{13}$$

$$d = [mS_1 \frac{(1 - cos2\alpha)}{2}]^{1/2} \tag{14}$$

Where, s = odd-bounce scattering, v = volumetric scattering, and d = even-bounce scattering.

The value of alpha (α) is in the range of 0 and π/2. If the value of α is equal to 0 then it shows surface scattering, if it is in the range of π/4 then it shows volume scattering and if it is equal to π/2 then it is double-bounce scattering.

CPR is a key parameter to determine the presence of water ice content on the lunar surface. It is defined as the
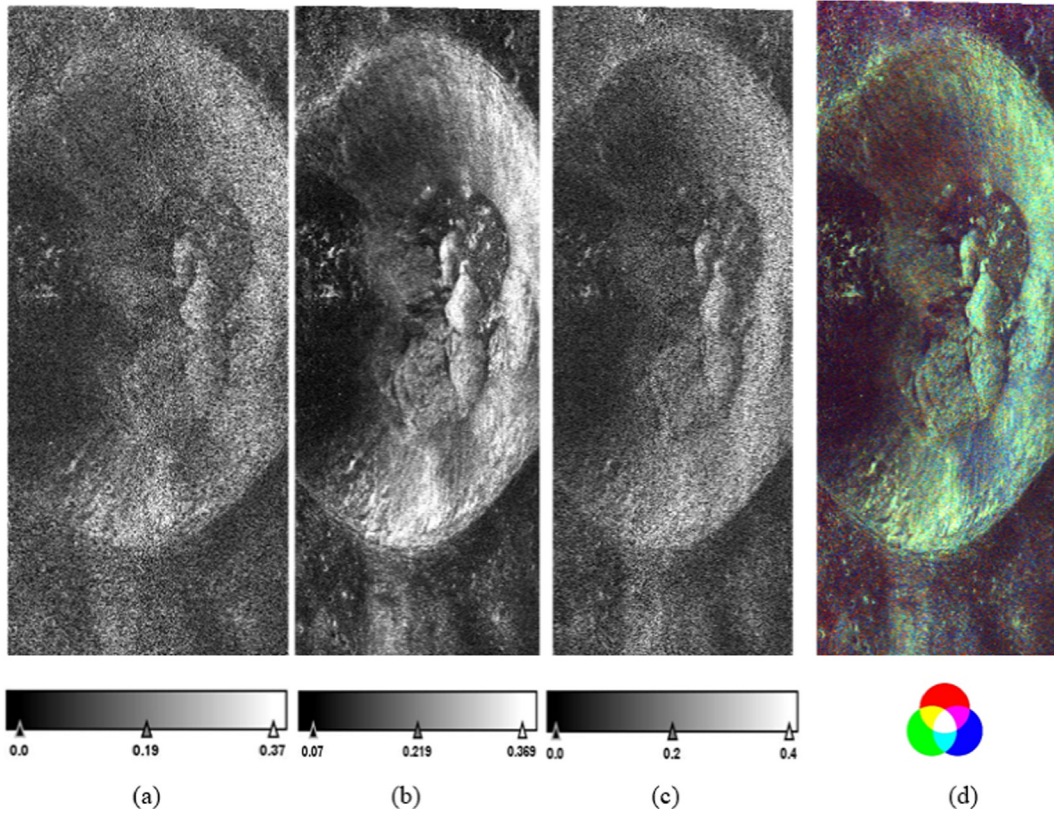
LRO (Mini-RF)

Fig. 5. m-delta decomposition of LRO (Mini-RF) (a) Double-bounce scattering, (b) Volume scattering, (c) Surface scattering, and (d) RGB color composite.

ratio between received power in the same sense (SC) to the transmitted in the opposite sense (OC) (Raney, 2007; Raney, 2006; Raney et al., 2021; Kumar et al., 2022a). CPR can be evaluated from the first and fourth Stokes parameters (Eq. (15)). Rough surfaces have a high CPR value which is more than unity as the incident radar wave bounces more than once which leads to more same sense (SC) signals resulting in high CPR. Usually, in surface scattering, the CPR value is less than unity.

$$CPR = (s_1 - s_4)/(s_1 + S_4) \qquad (15)$$

3.4. Dielectric constant

For this study, the dielectric constant is defined as a surface's response to an incident EMR, which is primarily in the microwave band. The attenuation factor (A_f) for this is defined mathematically as shown in Eq. (16) (Shukla, 2019; Vashishtha & Kumar, 2021).

$$A_f = exp\left(\frac{4\pi f \varepsilon'' d}{c\sqrt{\varepsilon'}}\right) \qquad (16)$$

In the above equation, f is the frequency of the incident electromagnetic wave, c is the velocity of the electromagnetic wave, the thickness of the surface is denoted by d and the complex dielectric constant is $\varepsilon = \varepsilon' - i\varepsilon''$.

The real part of a target surface's dielectric constant is just a density of the medium parameter, which is shown in the following Eqs. (17), (18) (Shukla, 2019; Shukla et al., 2019; Olhoeft and Strangway, 1975).

$$\varepsilon = (1.93 \pm 0.17)^\rho \qquad (17)$$

$$\tan\delta = 10^{0.038S + 0.312\rho - 3.260} \qquad (18)$$

The detailed equation parameters are derived in Shukla (2019), Shukla et al. (2019), and Olhoeft and Strangway (1975). In higher CPR values (>1), one can expect double-bounce scattering or volume scattering as a result of the small size particles made up of the lava flow (Calla et al., 2014b). As stated earlier that CPR is a key parameter to determine the presence of water ice content if the values of CPR are high (Calla et al., 2015; Mohan et al., 2013). The areas which show CPR less than unity act as a Braggs scattering surface (Shukla and Kumar, 2018). The presence of water ice can not be only confirmed by high CPR values as it could be due to surface roughness (Calla et al., 2016). The ice and regolith have similar dielectric properties which result in difficulty distinguishing radar returns (Fa et al., 2011; Spudis et al., 2013). Eke et al. (2014) also concluded that the craters which show areas having CPR more than unity can be due to the interaction of EMR to the boundary of water ice which suggests that the locations can be
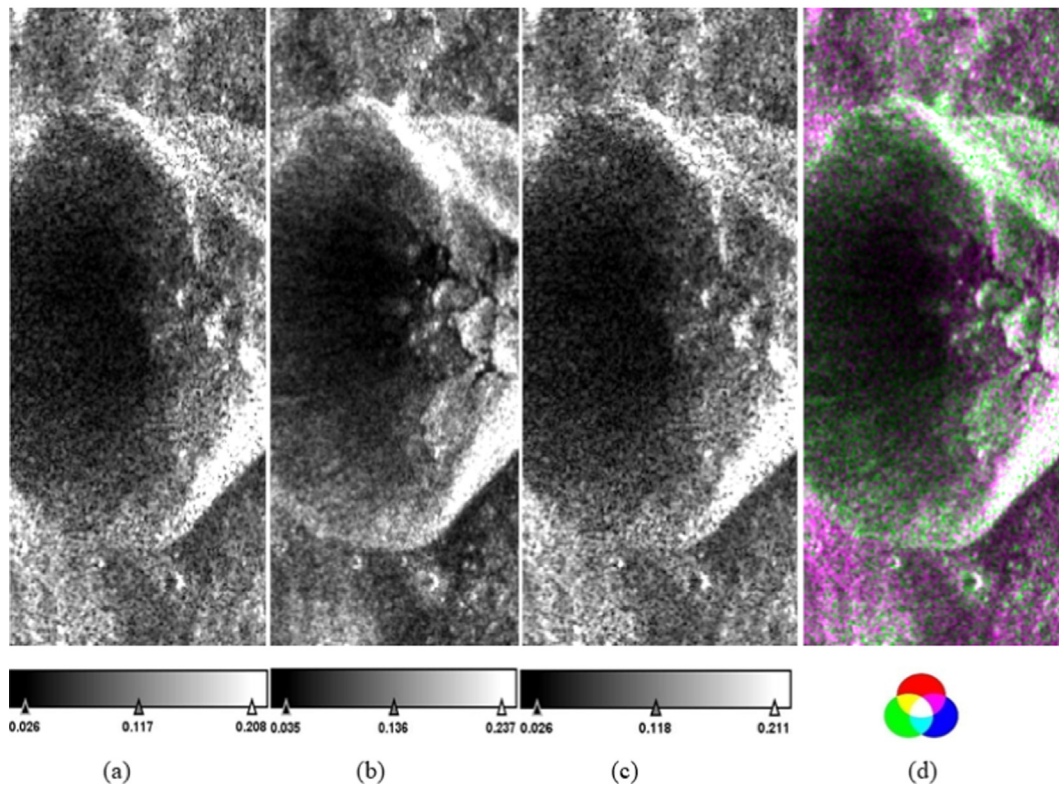
Chandrayaan-1 (Mini-SAR)

Fig. 6. m-chi decomposition of Chandrayaan-1 (Mini-SAR) (a) Double-bounce scattering, (b) Volume scattering,(c) Surface scattering, and (d) RGB color composite.

holding probable water ice deposits (Eke et al., 2014). Calla et al. (2016) showed using the Terrestrial Analogue of Lunar Soil (TALS), values of the dielectric constant were found to be fairly close to those observed at the Apollo-17 landing site, Taurus Littrow valley (Calla et al., 2014a, 2016). It was suggested by Calla et al. (2015) that the variation in received LH and LV components is affected by polarization states (same sense-SC and opposite sense-OC), as well as polarization parameters (m, delta-δ, chi-χ, CPR) (Calla et al., 2015).

The Apollo-17 mission was the final landing moon mission of the Apollo program in which the samples of the landing site Taurus Littrow valley were collected. The landing site is located at the coordinate 30°44′58.3″ east longitude by 20°9′50.5″ north latitude. The location of the site is quite interesting as Taurus and Littrow are the surrounding mountains and a crater respectively from which the name of the location site is derived from. The landing site is a part of the Serenitatis basin and is located on its southeastern rim. The landing site is surrounded by mountains or massifs which are north massif, south massif, and east massif (Wolfe et al., 1981). An interesting point to note is that a dark material is present on the surface of the floor and its composition shows that it is not part of the highland region of the moon, but it is of volcanic origin. The regolith of the landing is rich in basalt ejects, especially the uppermost part and is 1400 m thick (Wolfe et al., 1981). The last

Apollo mission also included the Lunar Roving Vehicle (LRV) and the Extravehicular Activity (EVA) done by it included the sample data collection. From the return samples and the experiments done in the laboratory, the maximum values of dielectric constants were calculated which were between 2 and 3.2 (Bhattacharya et al., 2015; Gold et al., 1976; Wolfe et al., 1981). Vashishtha & Kumar (2021) also calculated the dielectric values of this site from the Gaussian Model which came out to be 3.9867 in average value (Vashishtha & Kumar, 2021). The Gaussian model has been used in this study to determine the values of the dielectric constant. Calla et al. (2014a) also measured the values of the dielectric constant with the Terrestrial Analogue of Lunar Soil (TALS) which was around 3.61–4.22.

3.5. SAR backscatter modeling

The computed backscatter energy is dependent on various elements such as the dielectric constant, surface roughness, wavelength of EMR, frequency of EMR, incidence angle, and type of polarisation. Retrieving dielectric constant values from the radar backscatter coefficient is a difficult operation. As a result, separating the contributions of each of these components and determining the value of each factor is difficult. After computing the equations of theoretical empirical models to generate enormous data-
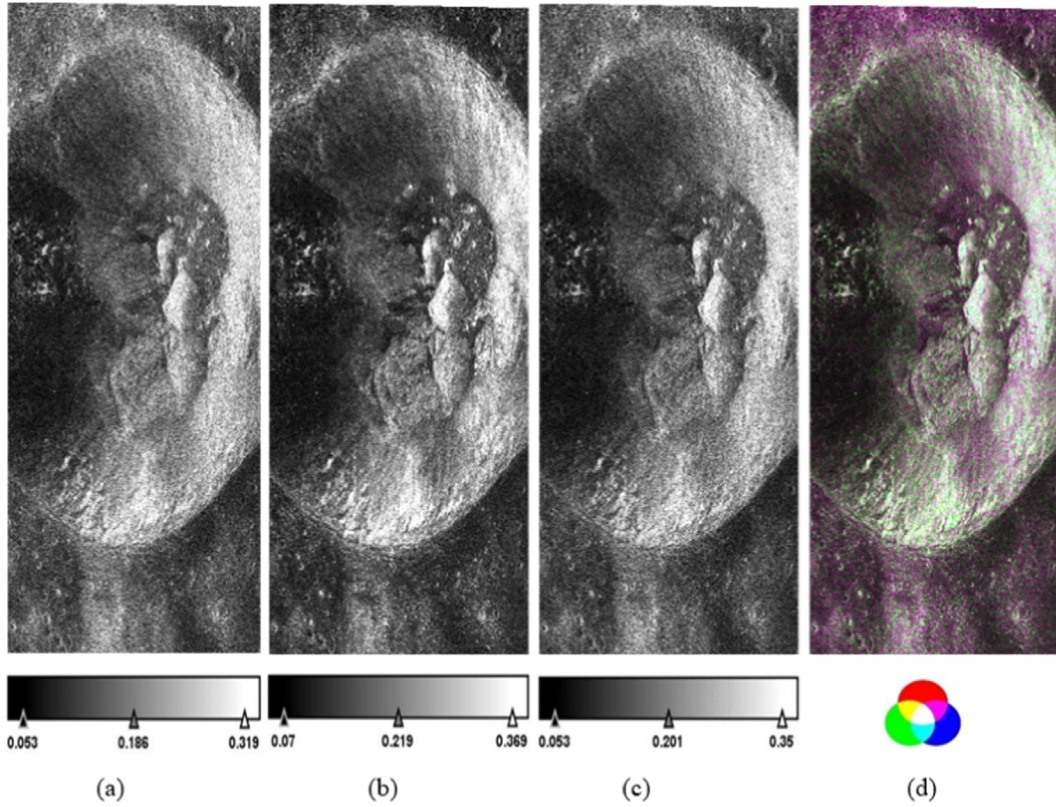
LRO (Mini-RF)

Fig. 7. m-chi decomposition of LRO (Mini-RF) (a) Double-bounce scattering, (b) Volume scattering, (c) Surface scattering, and (d) RGB color composite.

sets, any inversion approach is used to recover the value of any particular parameter, such as the dielectric constant in this work. Many electromagnetic backscattering models are available, such as the Kirchhoff Model, the Small Perturbation Model, and the Integral Equation Model (IEM), which can be used to generate simulated datasets. The range of roughness, which differs among different models, is the criterion for these models. To generate the simulated values in this work, the latest model IEM was used. IEM is a radiation transfer model based on a theoretical (physical) model. It is suitable for different roughness conditions and spatial independence by combining the Kirchoff model and the small disturbance model (SPM). Compared with other empirical models, this method is more suitable for extraterrestrial weathering layers, because its parameters depend on the location and have a wide range of surface roughness (Shahsavarhaghighi et al., 2013).

A.K Fung was the first to design the full version of the IEM model. It depends on a more detailed description of the integral equation of the electric field (Fa & Cai, 2013). The like-polarized backscattering coefficient σ^0 can be represented in the Integral Equation Model (IEM) (Shukla et al., 2019).

$$\sigma^0_{pp} = \frac{k^2}{2} e^{-2k_z^2 \sigma_h^2} \sum_{n=1}^{\infty} \frac{\sigma_h^{2n} |I^n_{pp}|^2 W^n(-2k_x, 0)}{n!} \quad (19)$$

Where,

$$I^n_{pp} = (2k_z)^n f_{pp} e^{-\sigma_h^2 k_z^2} + \frac{k_z^n \left[F_{pp}(-k_x, 0) + F_{pp}(k_x, 0) \right]}{2} \quad (20)$$

As a function of the Fresnel reflection coefficient, the IEM equation parameters f_{vv} and f_{hh} can be expressed as follows (Shukla, 2019).

$f_{vv} = 2R_v/\cos\theta$, $f_{hh} = -2R_h/\cos\theta$.

$$[F_{vv}(-k_x, 0) + F_{vv}(k_x, 0)] = \frac{2\sin^2\theta(1 + R_v)^2}{\cos\theta}$$
$$\times \left[\left(1 - \frac{1}{\epsilon}\right) + \frac{\epsilon - \sin^2\theta - \epsilon\cos^2\theta}{\epsilon^2\cos^2\theta} \right] \quad (21)$$

$$[F_{hh}(-k_x, 0) + F_{hh}(k_x, 0)] = -\frac{2\sin^2\theta(1 + R_h)^2}{\cos\theta} \left[\frac{\epsilon - 1}{\cos^2\theta} \right] \quad (22)$$

where, ϵ: complex dielectric constant, $k_z = k\cos\theta$, $k_x = k\sin\theta$.

R_h and R_v: Fresnel reflection coefficients for horizontal and vertical polarizations are given by Eqs. (23), (24).

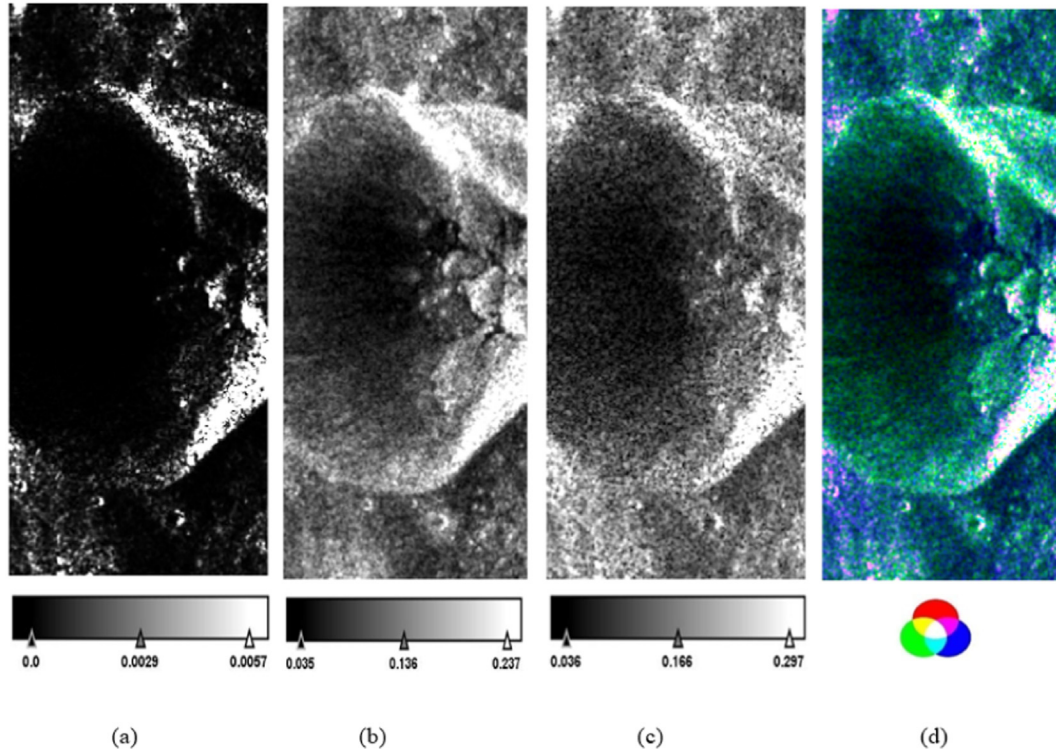$$R_h = \frac{\cos\theta - \sqrt{\epsilon - \sin^2\theta}}{\cos\theta + \sqrt{\epsilon - \sin^2\theta}} \quad (23)$$

Fig. 8. m-alpha decomposition of Chandrayaan-1 (Mini-SAR) (a) Double-bounce scattering, (b) Volume scattering,(c) Surface scattering, and (d) RGB color composite.

$$R_v = \frac{\epsilon \cos\theta - \sqrt{\epsilon - \sin^2\theta}}{\epsilon \cos\theta + \sqrt{\epsilon - \sin^2\theta}} \tag{24}$$

$W^n (u,v)$ is represented by the Fourier transform of the nth power of surface correlation function $\rho(x,y)$ and given by Eq. (25).

$$\mathbf{W^n(u,v)} = \frac{1}{2\pi} \int_{-\infty}^{\infty} \rho^n(x,y) e^{-jux - jvy} \mathbf{dxdy} \tag{25}$$

The Gaussian surface correlation functions are given by Eq. (26).

$$\rho(x,y) = e^{-\frac{x^2}{L_x^2} - \frac{y^2}{L_y^2}} \text{ (Gaussian)} \tag{26}$$

L_x and L_y are given by correlation length in the x and y directions.

A simulation was performed using Eqs. (19)-(26) and the simulated data were used for training the Artificial Neural Network (ANN) based model. Compact/Hybrid-pol Mini-SAR and Mini-RF data-based dielectric constant retrieval were performed using the Nonlinear Multi-Layer Percep-tron (MLP) Regression by Artificial Neural Network (ANN) as mentioned in the research carried out by Vashishtha & Kumar (2021). Backpropagation algorithm (as mentioned in Hayklin, 1994) that was performed on fully polarimetric L-band DFSAR data was used for model

fitting (Hayklin, 1994). The details of the algorithm for retrieval of dielectric values for Hermite-A crater using DFSAR data are given in Appendix B.

3.6. Decomposition models for the fully polarimetric dataset

For characterization of L-band DFSAR of Chandrayaan-2 fully polarimetric dataset, two decomposi-tions techniques have been used in this study namely Bar-nes Decomposition and H-A-Alpha decomposition. Barnes decomposition is based on the 'wave dichotomy' and H-A-Alpha decomposition is based on eigenvalue and eigenvector (Kumar et al., 2022a). The use of these two decompositions in this study was to minimize the over-estimation of particular scattering (Shafai & Kumar, 2020; Bhanu Prakash & Kumar, 2021a, 2021b; Ramya & Kumar, 2021) in a target area which is easily seen in the model-based decomposition techniques.

Initially, for L-band data, the calibration was performed on the polarimetric channels of SLC data at the linear scale. The radiometric calibration of the DFSAR data was performed using Eq. (27) (Bhiravarasu et al., 2021; Kumar et al., 2022a).

$$\sigma^0(linear) = \frac{DN_{i,j}}{10^{\frac{k}{10}}} \tag{27}$$

4. Results and discussion

4.1. Characterization of Hermite-A crater

Hermite-A crater is a small crater which is situated near the Hermite crater in the North Pole. Hermite-A does lie in the PSR region. The characterization of this crater is on three decomposition techniques and CPR for Hybrid-Pol data of Chandrayaan-1 and LRO which is of S-band. For Fully polarimetric data of DFSAR of Chandrayaan-2, the Barnes decomposition technique and H-A-α decomposition technique has been used to analyze the different scattering mechanisms and polarimetric parameters including the CPR.

4.1.1. m-δ (m-delta) decomposition

In this decomposition, the analysis is being made based on three scattering mechanisms which are surface, double-bounce, and volume scattering. The RGB composite image from all these scattering mechanisms has been made for the crater to analyze the scattering pattern and the extent of ejecta around the rim of the crater. The colors like cyan, magenta, and yellow have been included to indicate the mixing of the scattering patterns.

Fig. 4 shows the RGB composite of the m-δ decomposition of the Hermite-A crater of Mini-SAR of Chandrayaan-1 data which shows the dominance of volume scattering in the crater walls, whereas the crater base and the surrounding area around the rim show the dominance of surface scattering and double bounce scattering. The crater base and the surrounding areas are smooth, so the surface scattering is more prominent in these regions. The small peak present in the crater floor depicts volume scattering. Double-bounce scattering is visible in the crater base and outside the crater rim which can be because of the natural dihedral structure in the surroundings. The mean values of volume scattering are 0.136, for surface scattering, it is 0.125 and for double-bounce scattering, it is 0.117.

Fig. 5 shows the RGB composite of the m-δ decomposition of the Hermite-A crater seen from Mini-RF from LRO, which shows that the dominance of volume scattering is found in the crater walls suggesting that the walls of the crater are of the rough surface as it was seen in m-δ decomposition and the m-χ decomposition of the Mini-SAR data. The crater base also has double-bounce and surface scattering in some of the regions, but the small peak present in the crater base is showing volume scattering and some of the regions of the crater walls are showing
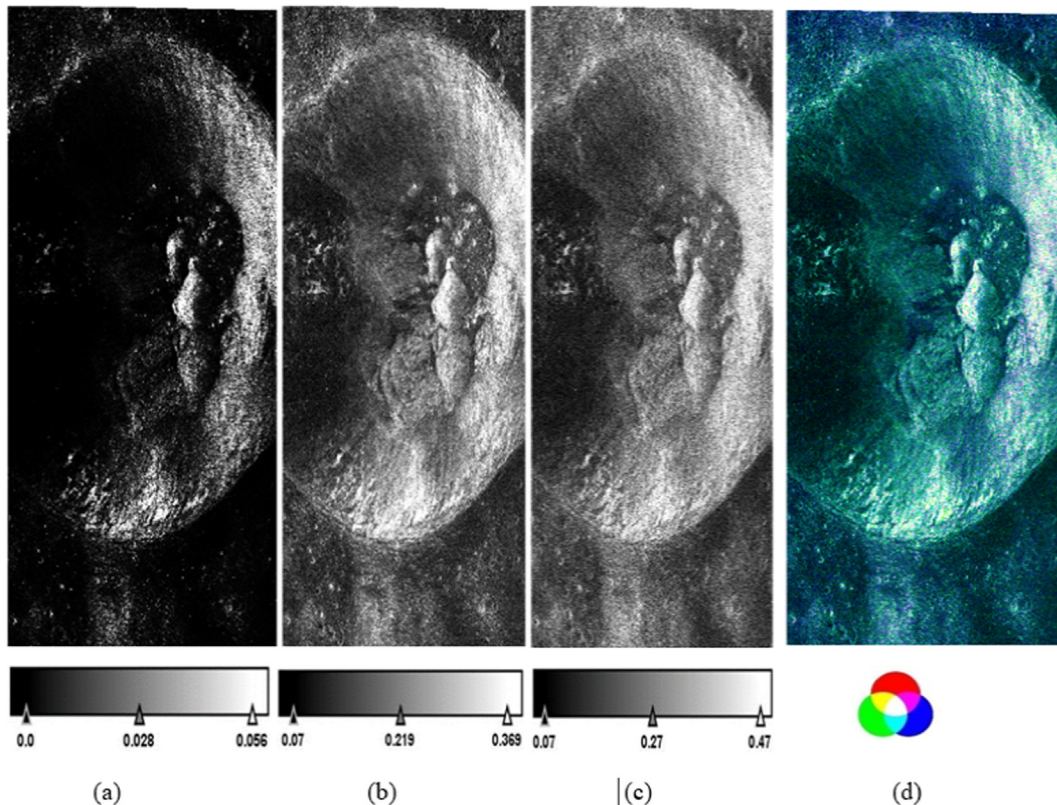
LRO (Mini-RF)

Fig. 9. m-alpha decomposition of LRO (Mini-RF) (a) Double-bounce scattering, (b) Volume scattering, (c) Surface scattering, and (d) RGB color composite.

both double-bounce and surface scattering elements. The crater walls are clearly showing all the scattering and the crater walls, but volume scattering is seen as dominant. The Magenta color in the crater base and the surrounding around the rim show the combination of double-bounce and surface scattering. The mean values of the volume scattering are 0.219 and for the double-bounce is 0.19 which is the lowest and for surface scattering is 0.2.

4.1.2. m-chi decomposition

Fig. 6 shows the RGB composite of the m-χ decomposition of the Hermite-A crater seen from Mini-SAR data of Chandrayaan-1, which shows that the dominance of volume scattering is found in the crater walls suggesting that the walls of the crater are of the rough surface as it was seen in m-δ decomposition. The crater base has double-bounce and surface scattering as in dominance, but the small peak present in the crater base is showing volume scattering. The crater walls are clearly showing all the scattering and the crater walls are much more visible in this decomposition technique in comparison to the m-delta decomposition. The Magenta color in the crater base and the surrounding around the rim show the combination of double-bounce and surface scattering. The mean values of the volume scattering are 0.136 and for double-bounce is 0.117 and surface scattering is 0.118 which is nearly the same.

Fig. 7 shows the RGB composite of the m-χ decomposition of the Hermite-A crater seen from Mini-RF from LRO, which shows that the dominance of volume scattering is found in the crater walls suggesting that the walls of the crater are of the rough surface as it was seen in m-δ decomposition and the m-χ decomposition of the Mini-SAR data. The crater base also has double-bounce and surface scattering in some of the regions, but the small peak present in the crater base is showing volume scattering and some of the regions of the crater walls are showing both double-bounce and surface scattering. The crater walls are clearly showing all the scattering and the crater walls, but volume scattering is seen as dominance. The Magenta color in the crater base and the surrounding around the rim show the combination of double-bounce and surface scattering. The mean values of the volume scattering are 0.219 and for double-bounce is 0.186 which is the lowest and for surface scattering is 0.201.

4.1.3. m-alpha decomposition

Fig. 8 shows the RGB composite of m-α decomposition of Hermite-A crater seen from Mini-SAR data of Chandrayaan-1, which shows that the dominance of volume scattering is found in the crater walls suggesting that the walls of the crater are of the rough surface as it was seen in m-δ and m-χ decomposition. High volume scattering is seen in the crater walls as it was seen in the other two decompositions i.e., m-δ and m-χ. But in this, the crater base shows the dominance of surface scattering, and it is also seen on the outside of the crater rim. A very small scat-

tering of double bounce is seen in the rim connected to the crater which can be because of the presence of natural dihedral in the region. The peak in the crater base also shows the volume scattering. The small craters in the region outside the crater also show volume scattering whereas, the surface scattering outside the crater shows the area to be smooth which was not in the case of the other two decompositions. The mean values of volume scattering are 0.136 which is similar to all the decompositions and the surface scattering is 0.166 which is higher than the volume scattering whereas the mean values of double scattering are very low.

Fig. 9 shows the RGB composite of the m-α decomposition of the Hermite-A crater seen from Mini-RF from
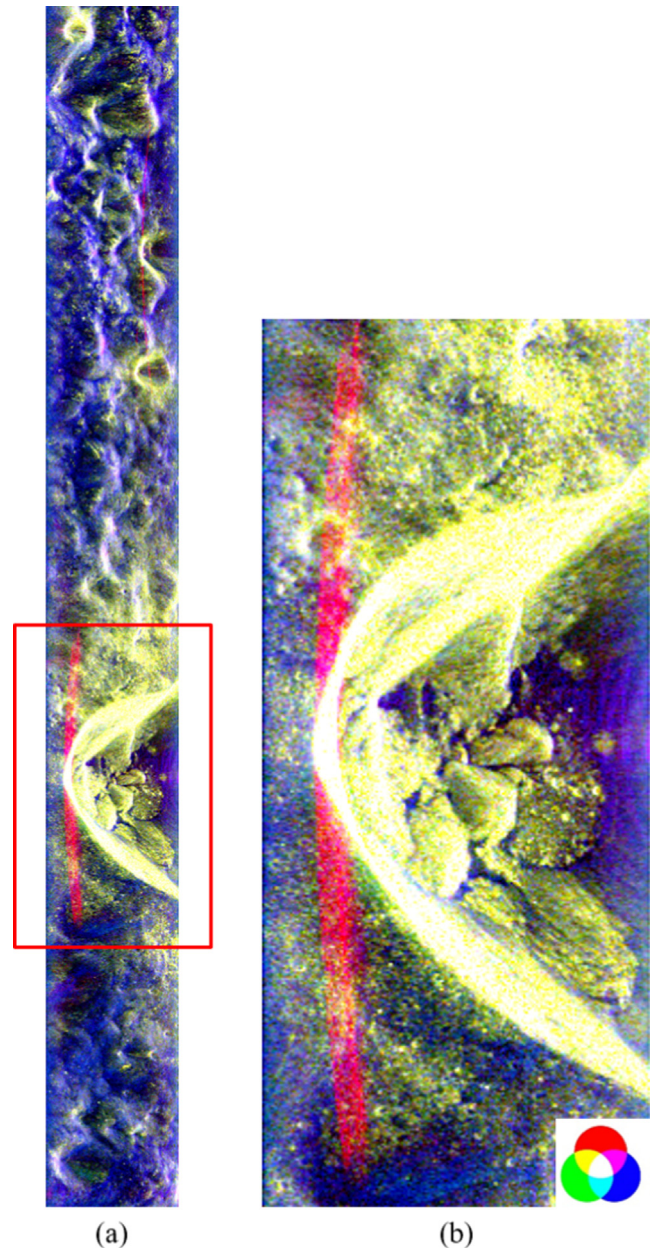

Fig. 10. Barnes decomposition for Chandrayaan-2(DFSAR) (a) Full scene of the data covering Hermite-A crater (b) Zoomed view of Hermite-A crater.
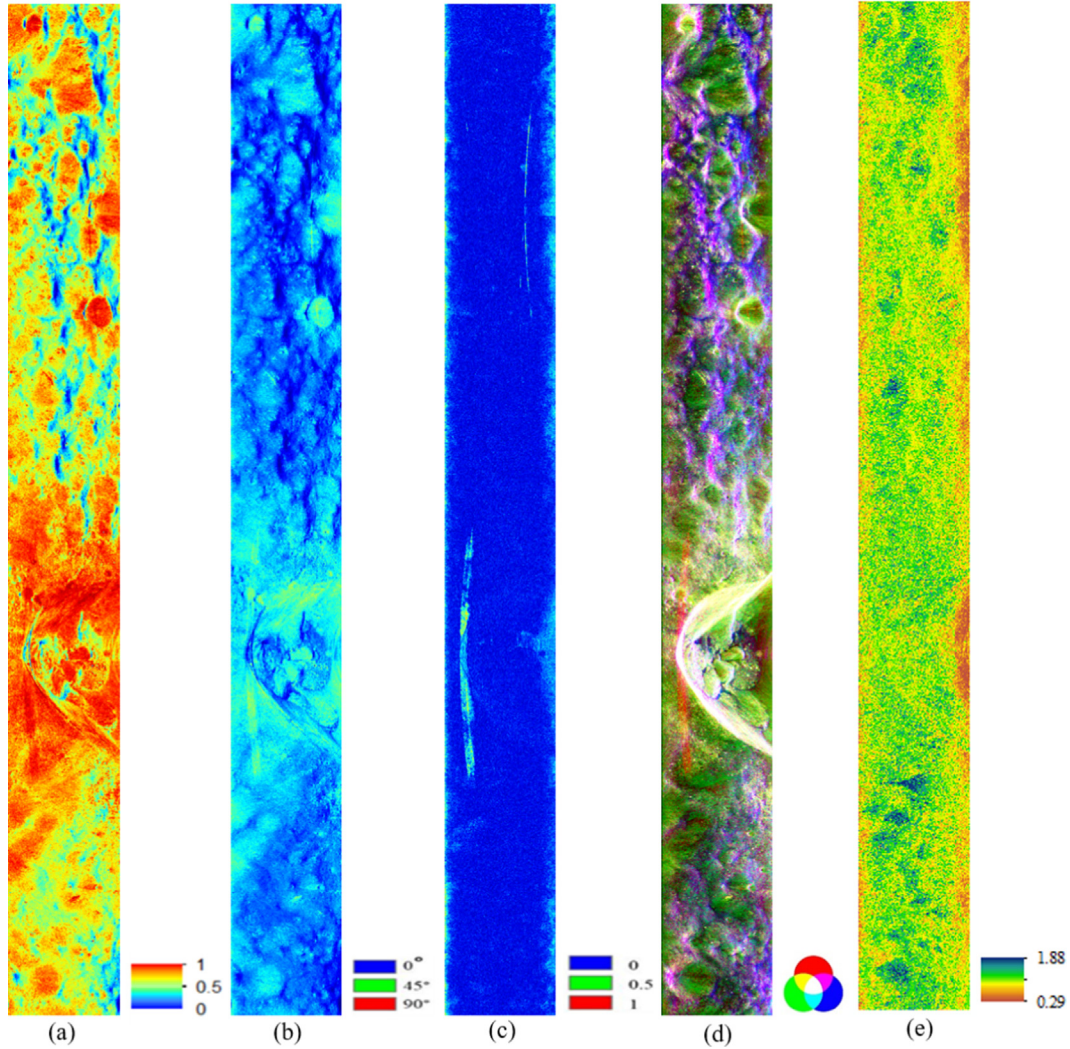
Fig. 11. Parameters of eigenvalue and eigenvector based decomposition and polarimetric decomposition (a) Entropy, (b) Alpha angle, (c) Anisotropy (d) H-A-Alpha decomposition (e) CPR.

LRO, which shows that the dominance of volume scattering is found in the crater walls suggesting that the walls of the crater are of the rough surface as it was seen in m-δ decomposition and the m-χ decomposition of the Mini-SAR data. The crater base shows surface scattering in some of the regions, but the small peak present in the crater base is showing volume scattering and some of the regions of the crater walls are showing surface scattering, making double-bounce scattering visibility low in the region. The region outside the crater shows the dominance of surface scattering and the smooth surface in the crater walls also depicts surface scattering. The mean values of the volume scattering are 0.219 and for surface, scattering is 0.27 and for the double bounce is 0.028 which is very low in comparison to the volume and double-bounce.

4.1.4. Barnes decomposition

Fig. 10 shows the RGB composite image of the Hermite-A crater highlighted in the red box (Fig. 10(a)) in the left image, which is Barnes decomposition for the DFSAR of Chandrayaan-2 data in the L-band. This decomposition shows the crater in a very good perspective in comparison to the S-band of Mini-SAR and Mini-RF of Chandryaan-1 and LRO respectively. The volume scattering is seen in dominance in the crater walls and the ejecta outside the crater rim (Fig. 10(b)). Some parts of the crater floor are showing surface scattering which was also seen in the S-band earlier depicting the crater floor is smooth. But the peaks situated inside the crater show volume scattering. The ejecta outside the crater rim can be easily identified in this scene as it is showing the extent of the ejecta to a good level. The craters which are seen in this scene can also be identified as it is showing volume scattering. The regolith or the lunar floor is showing surface scattering which is in blue depicting the surface to be smooth in the regions where the area of the crater is not present. Double bounce scattering is not seen but it is seen as a mixed scattering with the other scattering in some regions.
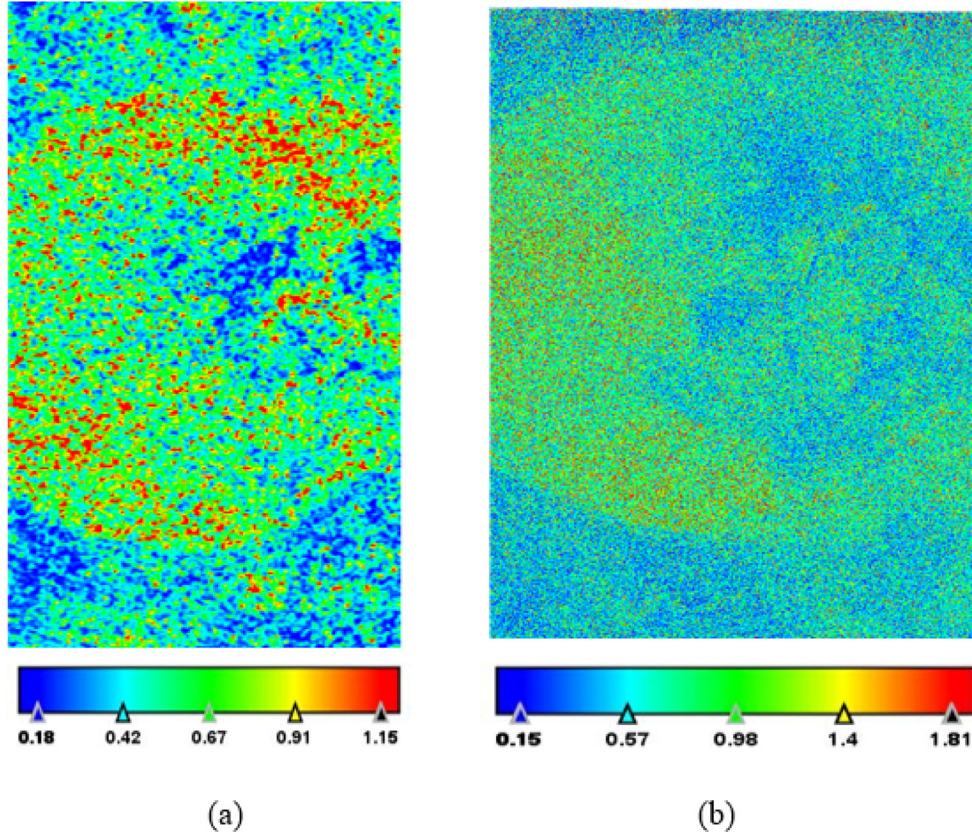
Fig. 12. Value of CPR for Hermite-A crater (a) Chandrayaan-1(Mini-SAR) (b) LRO (Mini-RF).

4.1.5. H-A-alpha decomposition

Fig. 11 shows the Entropy, Alpha, and Anisotropy derived from the H-A-alpha decomposition. These are the polarimetric parameters that are used to characterize the Hermite-A crater. The RGB composite image of the H-A-Alpha decomposition (Fig. 11(d)) has also been used to differentiate the scattering present in the scene and the crater. As it was seen in the Barnes decomposition (Fig. 10) of this scene, the crater gives the dominance of the volume scattering present in the walls and the floor of the crater which is in green color. The peaks situated at the crater floor and the parts of the crater wall also show volume scattering. This gives an interpretation of the rough surface present in the crater. A very small portion of the crater floor gives surface scattering and a mix of double bounce scattering in the crater floor. This gives an idea about the crater floor which is smooth on the surface in comparison to the crater walls. The other small craters in the scene are also identified which gives volume scattering and the area which is in blue gives the interpretation of the scattering from the smooth surface, which is surface scattering. The eigenvector-eigenvalue parameters Entropy and Alpha angle also go well with the results obtained from Barnes decomposition and H-A-Alpha decomposition models. The entropy values in the crater are higher and are around 1 in the crater region (Fig. 11(a)), which corresponds that it is because of the volume scattering present in the crater.. It was also seen that the entropy values were higher in the regions where volume scattering was high which was in the crater walls and the peaks situated at the crater floor and crater walls. The value of the alpha angle is around 45° in the crater region (Fig. 11(b)), which again corresponds to volume scattering present in the crater. This supports the results of the decomposition technique obtained in the form of the dominance of volumetric scattering. The value of Anisotropy in the major portion of the crater is zero (Fig. 11(c)), which represents that the scattering is obtained from three pure targets. Fig. 11(e) also shows the value of CPR obtained from the DFSAR datasets for the Hermite-A crater. The CPR was obtained from the simulated/hybrid pol SAR data for this. High CPR values of more than 1 could be easily seen in the crater. The crater shows CPR values of around 1.5 on the left side of the crater walls. The crater walls show volume scattering in both of the decomposition techniques (Barnes and H-A-alpha) performed on the datasets. This indicates that the regions of the crater show high volume scattering along with the high values of CPR. With these results, it can be withdrawn that the crater shows volume scattering in both the datasets and high CPR values on the decomposition models that were applied.

4.1.6. Analysis of CPR

Fig. 12 (a) shows the values of CPR from the Mini-SAR of Chandrayaan-1 in the crater. The high values of CPR, which is more than 1 in the Hermite-A crater depict that
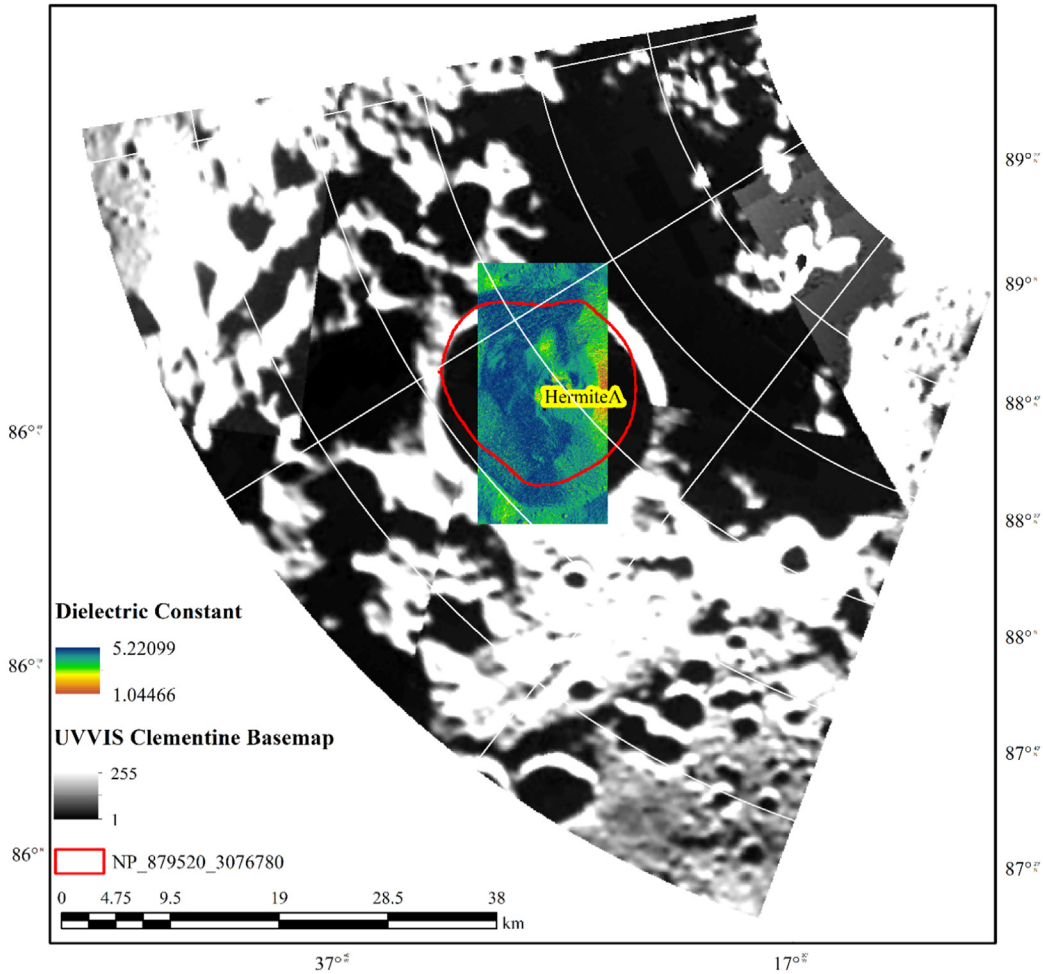
Fig. 13. IEM-based dielectric constant values of Hermite-A crater using S-band Chandrayaan-1 Mini-SAR data.

the crater has some areas which can be a probable location of water ice deposits. The values which are below 1 relate to the lunar regolith and other materials. The high values of CPR can be also due to the scattering by the rough surface, which can be because of double bounce scattering or volume scattering. The locations of the crater walls show high CPR which is close to 1.15, particularly in the crater walls on the left side and some areas on the floor of the crater. The areas outside of the crater show a low CPR value which can be caused due to the surface scattering. Fig. 12 (b) shows the value of CPR which is seen from the Mini-RF of LRO data of Hermite-A crater. Here, the value of CPR is much higher in comparison to the Mini-SAR. The values are near 1.81 on the left of the crater walls and in some areas on the floor of the crater. The value of around 1.4 is also seen in those areas which are also quite higher in these regions in comparison to the Mini-SAR data. Here, the lowest value is less than the Mini-SAR which is around 0.15 which depicts the region of surface scattering which is present on the crater floor and the areas outside the crater. It can be seen that the region where the value of the CPR is more than 1 those regions showed volume scattering in the decomposition.

4.2. Dielectric characterization of Hermite-A crater

Fig. 13 shows the map of the dielectric constant values of the Hermite-A crater from the Mini-SAR of Chandrayaan-1 data with the Clementine base map in the background. The red encircled area shows the PSR of the crater with the PSR Id NP_879520_3076780. The materials with the dielectric constant value of 3.17686 lie in the range of the dielectric constant of water-ice in the left, center, and right sides of the crater The middle part of the crater shows the crater base and the right side of the crater shows the region of the crater walls. A surface ice cluster may be responsible for the dielectric constant of 3 in these areas. The high values shown in crater walls on the right can be because of surface ice clusters or radar look direction. This can be further explored in future exploratory missions. There are some regions too that show the dielectric constant values around 3 but, when compared with the m-chi decomposition of the same region, they do not show volume scattering in these regions. So, it can be noted that these locations are not the possible locations of water ice deposits.

Fig. 14 shows the map of the dielectric constant values of the Hermite-A crater from Mini-RF LRO data with
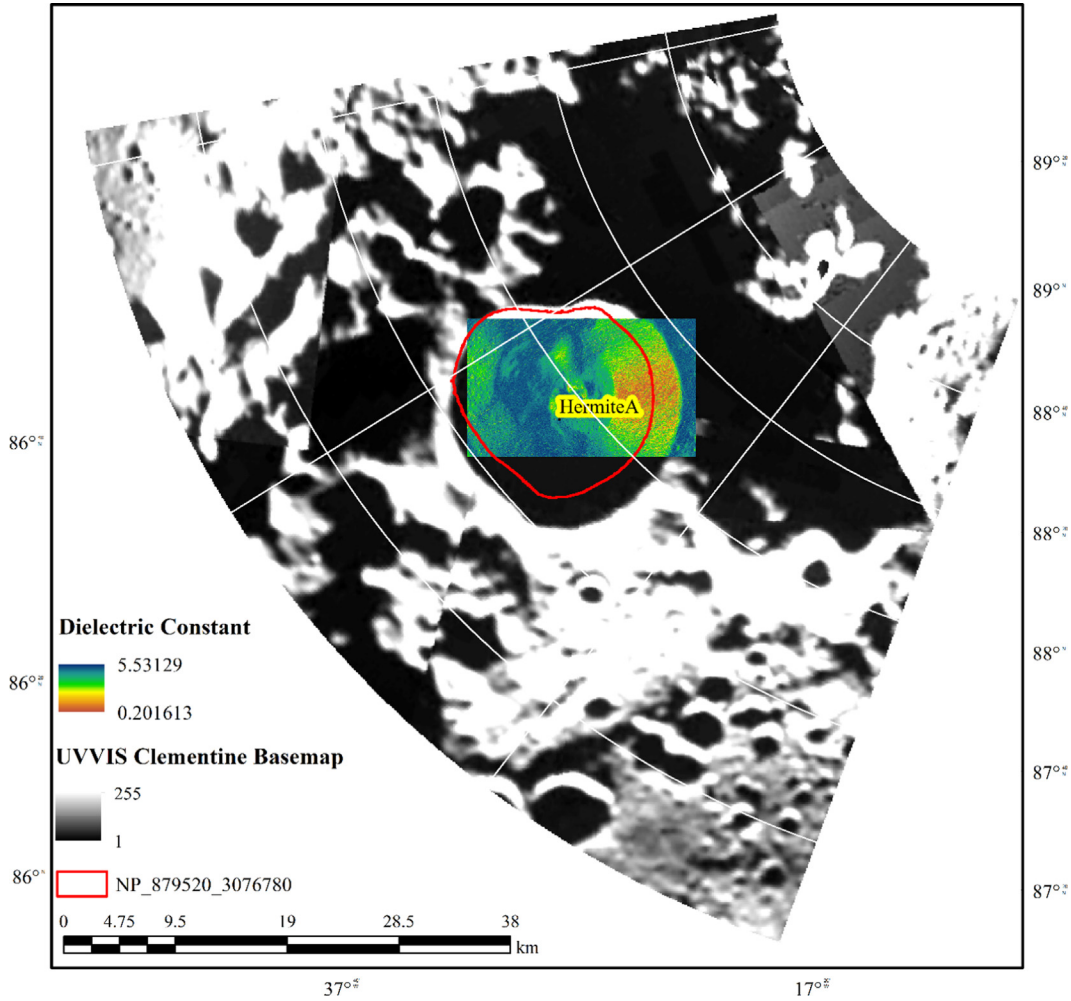
Fig. 14. IEM-based dielectric constant values of Hermite-A crater using S-band LRO Mini-RF data.

the Clementine base map in the background. The red encircled area shows the PSR of the crater with the PSR Id NP_879520_3076780. The values of the dielectric constant which is 3.18476 lie in the range of the dielectric constant of water-ice in locations on the left, center, and right sides of the crater. The middle part of the crater shows the crater base and the right side of the crater shows the region of the crater walls. A surface ice cluster may be responsible for the dielectric constant of 3 in these areas. The high values shown in crater walls on the right can be because of surface ice clusters or radar look direction which can be explored further in future missions. So, these locations of the crater can be probable locations of water ice deposits. In the study, Fa et al. (2011) proposed a model with several modeling parameters for it and one of the parameters includes the dielectric constant of the water ice which should be around $3.15 + i(0.0001–0.1)$ (Fa et al., 2011). As the range of dielectric constant for both of the sensors is around 3 for the Hermite-A crater, it can be said that these locations may be having water-ice deposits. The range of dielectric constant derived from the Mini-SAR

of Chandrayaan-1 and Mini-RF of LRO is pretty similar which is 1.04466 to 5.22099 and 0.2016 to 5.53129. The relationship between CPR of Mini-SAR and Mini-RF with other polarimetric parameters like degree of polarization (m), relative phase (δ), ellipticity parameter (χ) and polarization angle (α) did not give any meaningful relationship between them.

The dielectric values of the Hermite-A crater may further be investigated with the help of dual-frequency SAR and other available sensor datasets.

Fig. 15 shows the map of the dielectric constant values of the Hermite-A crater from the DFSAR of Chandrayaan-2 data with the Clementine base map in the background. The red encircled area shows the PSR of the crater with the PSR Id NP_879520_3076780. To cover the maximum area of the crater, the mosaic of two scenes of the SRI product was used (ch2_sar_nrxl_20191019t011 733461_d_fp_d18 and ch2_sar_ncxl_20191116t220423370_ d_fp_d18). The dielectric constant for the DFSAR data-based Integral Equation Model (IEM) in which the Gaussian model has been used to retrieve the values of the
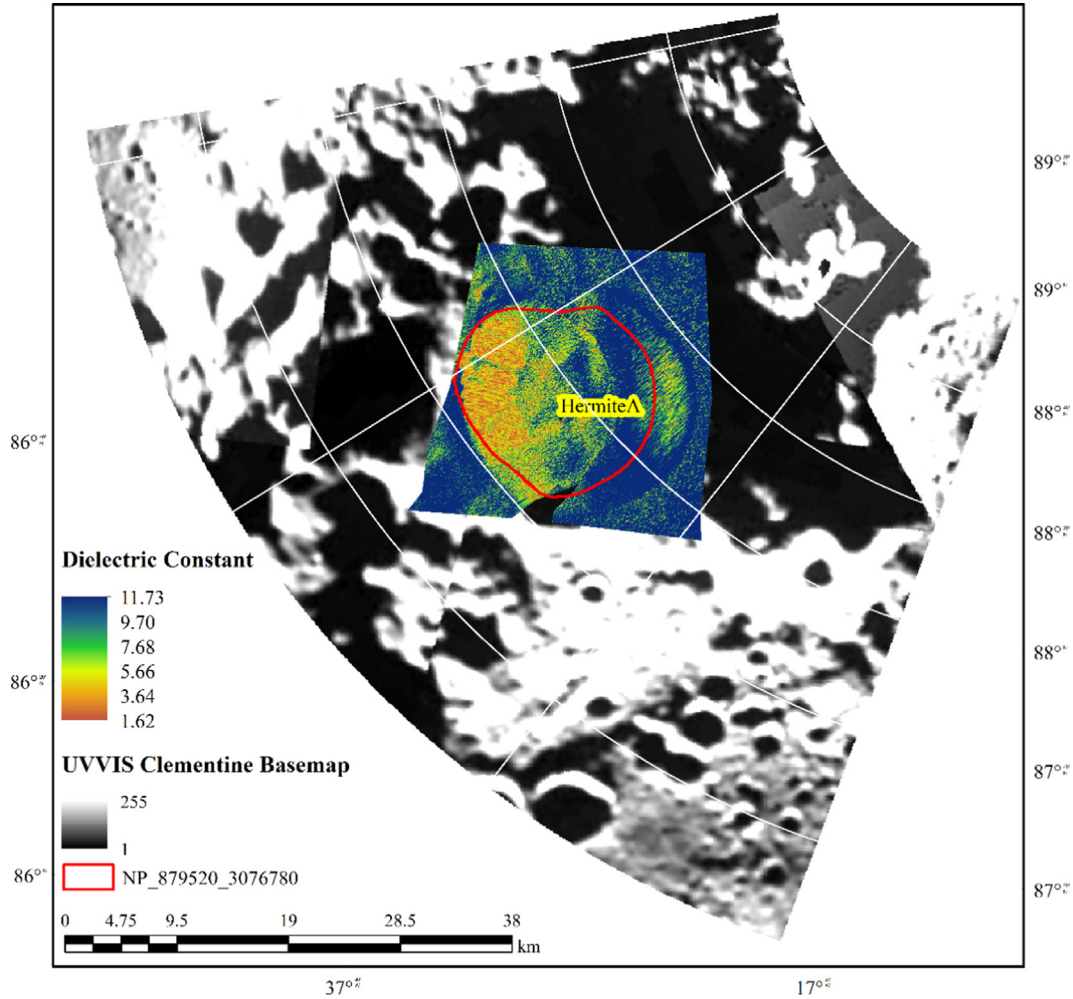
Fig. 15. IEM-based dielectric constant values of Hermite-A crater using L-band DFSAR Chandrayaan-2 data.

dielectric constant. The materials with the dielectric constant value of 3.64 to 5.66 lie in the range of the dielectric constant of the water-ice on the left of the crater. The middle part of the crater shows the crater base and the right side of the crater shows the region of the crater walls which show high values of dielectric constant in blue and the range is around 7.68 to 11.73. Though the highest value of the dielectric constant is around 11.73 on the crater floor and some parts of the crater walls on the right side, most of the crater floor and the left side of the crater walls have lower values which lie in the range of dielectric constant values of water ice. A small portion of the wall on the right side of the crater show values of 5.66 to 7.68, in which small patches can be seen having values around 3.64. The high values of the dielectric constant may be because of the slope of the crater and the incidence angle of SAR datasets. Further analysis can be made with the S-band of DFSAR Chandrayaan-2 of the same region and can be compared along with the S-band of Mini-RF of LRO and Mini-SAR of Chandrayaan-1.

A recent study shows the distribution of ice clusters present in the lunar north pole (Li et al., 2018). Various studies

in the past that have been carried out state the importance of CPR for water ice detection on lunar poles (Nozette et al., 2001; Spudis et al., 2013; Thomson et al., 2012). It may be possible for regions where CPR values are greater than unity to be caused by EMR interacting with the boundary of water ice and hence may be possible locations of water ice deposits (Eke et al., 2014). It can also be concluded that values of high CPR may be possible because of the lunar boulders or the rough surface present in the lunar regolith (Fa & Cai, 2013). It is a bit difficult to conclude that the detection of the water-ice present in the regolith is because of the high values of CPR. As high volume scattering is also present in the crater and it is clear in all the decomposition techniques. A recent study which was carried out by Li et al. (2018) showed the distribution of ice clusters in the region (Li et al., 2018) (Fig. 16) from the Moon Mineralogy Mapper (M3) aboard Chandrayaan-1 which shows Hermite-A crater in the encircled region and it can be seen that the surface ice clusters are present in the walls. So, it can be concluded from the results that the high volume scattering and high CPR and the values of dielectric constant which lie in the range of water-ice
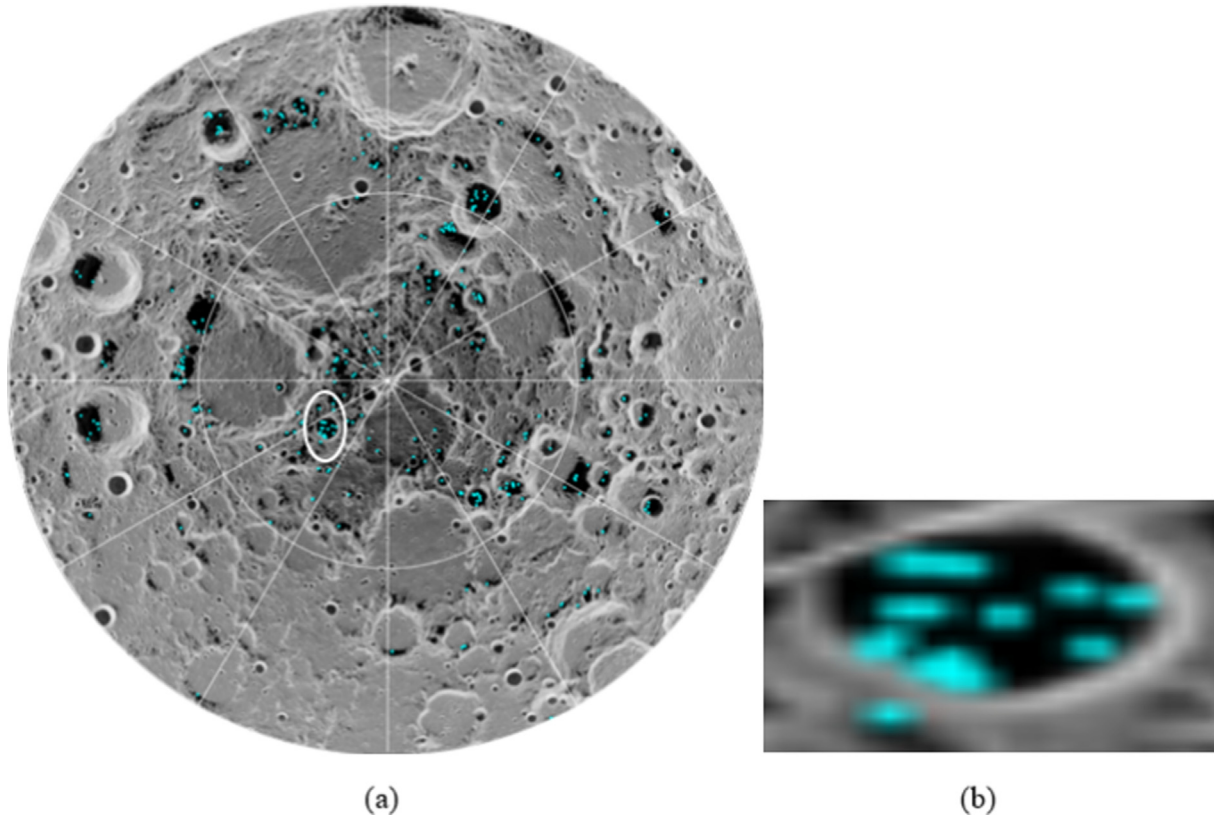
Fig. 16. Clusters of surface ice at the Lunar North Pole, detected by NASA's Moon Mineralogy Mapper instrument of ISRO's Chandrayaan-1 mission (Credit: NASA). (a) The white circle is the Hermite-A crater (b) Zoomed view of the Hermite-A crater.

which is around $3.15 + i(0.0001–0.1)$ are not because of boulders or rocks but it may also be due to the presence of water-ice present in the regolith of the crater (Fa et al., 2011).

5. Conclusions

The main objective of this research is to utilize compact and fully polarimetric SAR data for dielectric characterization of the Hermite-A crater and comparison with the map of ice clusters that were generated in the previous studies for the permanently shadowed region which was done with the combination of the polarimetric parameters, decomposition techniques, and dielectric constant values. To achieve this objective the m-delta, m-chi, and m-alpha decomposition have been used for the Hybrid polarimetric data and Barnes decomposition and eigenvector and eigenvalues based H-A-Alpha decomposition model have been used for fully polarimetric data. The scattering patterns that were obtained from these decompositions were supported by Entropy, Alpha angle, and Anisotropy parameters. The dielectric constant values also supported these patterns. The crater showed very high volume scattering in the walls of the crater and which was obtained in all the decompositions applied to the scenes. The value of the

CPR was also more than unity in the regions where the volume scattering was high in all the datasets used. The dielectric constant values of the water-ice in the crater were in the optimum range which is around 3 in the regions where the volume scattering was high and the values of CPR were high. The values of the dielectric constant for L-band DFSAR data of Chandrayaan-2 were relatively higher than the Mini-SAR and Mini-RF data but, there were some regions whose values were in the range of 3 on the left side of the crater walls. The region was also compared with the surface ice distribution map done by Li et al. (2018), it is found that the reason for getting high volume scattering and high CPR and the dielectric constant of water ice was also in the range and it is because of the water-ice present in the PSR of the lunar north polar crater. From all the above conclusions made from the study, it is clear that the part of the areas of Hermite-A crater can have probable locations of water ice deposit and future explorations can be done to identify those areas of the crater with in-situ experiments on the lunar surface. For the dielectric characterization of the Hermite-A crater, fully polarimetric L-band DFSAR datasets of the Chandrayaan-2 mission and compact/hybrid polarimetric Mini-RF and Mini-SAR datasets of LRO and Chandrayaan-1 missions have been used in this study. The potential of fully polarimetric

L- and S-band data of the DFSAR sensor should be used for the detection of surface ice clusters by including lunar regolith's dielectric behavior and dual-frequency PolSAR-based scattering properties in the permanently shadowed regions in addition to geomorphological parameters and in-situ measurements.

Authors Contributions

Mr. Awinash Singh (**AS**) contributed to original draft writing, methodology, identification of permanently shadowed regions (PSRs), satellite data selection, polarimetric SAR data processing, validation, writing— reviewing, and editing. **Ms. Aanchal Sharma** (**AS**) contributed to the Integral Equation Model (IEM) for dielectric characterization of Hermite-A Crater using L-band DFSAR data of Chandrayaan-2, mosaic creation of L-band DFSAR data for the lunar North Pole using 60 SRI products, dielectric map creation of Mini-SAR & Mini-RF data, and polarimetric processing of L-band DFSAR data. **Dr. Shashi Kumar** (**SK**) contributed to the supervision of the research work, investigation of the project work, the conceptualization of the methodological framework, data selection, software, radiometric calibration, polarimetric SAR data processing, analysis of the results, validation, writing— reviewing, and editing. **Dr. Ling Chang (LC)** contributed to the supervision of the research work, and reviewed and edited the draft. **Ms. Ankita Vashishtha** (**AV**) contributed to the Integral Equation Model (IEM) for dielectric characterization of Hermite-A Crater using Chandrayaan-1 and Lunar Reconnaissance Orbiter (LRO) data. **Dr. Rahul Raj** (**RR**) contributed to reviewing and editing the draft. **Ms. Shefali Agrawal (SA)** is involved in project management. **Dr. Prakash Chauhan** (**PC**) is involved in project management and administration. Dr. Prakash Chauhan made significant and valuable suggestions to identify PSR locations for polarimetric analysis of DFSAR data and dielectric characterization of PSR. All the authors have read and agreed to the published version of the manuscript.

Declaration of Competing Interest

The authors declare that they have no known competing financial interests or personal relationships that could have appeared to influence the work reported in this paper.

Acknowledgement

Appendix A.   See Table A1.

Table A1

Description of Chandrayaan-2 mission's L-band DFSAR data that were used to generate the mosaic for the lunar North Pole, as shown in Fig. 1.

Product name	Date of acquisition	Line/pixel Spacing (meters)	Azimuth & Range Resolution (meters)	Look angle (degrees)	Scene center coordinates (Lat & Long)	Spacecraft altitude (meters)
ch2_sar_ncxl_20190927t084045646_d_fp_d18	27-09-2019	0.550128, 9.593359	10.806951, 19.986164	26.014494	82.931296, −75.382467	107,381
ch2_sar_ncxl_20190927t004913859_d_fp_d18	27-09-2019	0.548935, 9.593359	10.806763, 19.986164	26.002062	82.90285, −72.068359	107,412
ch2_sar_ncxl_20190928t061731393_d_fp_d18	28-09-2019	0.533676, 9.593359	11.461908, 19.986164	26.001711	82.093898, −84.263099	104,281
ch2_sar_nrxl_20191009t132320814_d_fp_d18	9/10/2019	0.576534, 9.593359	11.475, 19.986164	26.00119	84.26193, 117.559828	114,020
ch2_sar_nrxl_20191012t160410765_d_fp_d18	12/10/2019	0.581692, 9.593359	10.8, 19.986164	26.000105	88.298004, 69.782136	115,115
ch2_sar_nrxl_20191012t215748426_d_fp_d18	12/10/2019	0.580213, 9.593359	11.475, 19.986164	26.000289	88.322857, 66.561263	114,685
ch2_sar_nrxl_20191014t190846230_d_fp_d18	14-10-2019	0.486244, 9.593359	13.5, 19.986164	25.997859	87.730314, 39.231134	117,994
ch2_sar_ncxl_20191016t003658177_d_fp_m65	16-10-2019	0.583254, 9.593359	10.122075, 19.986164	25.998085	87.95326, 15.159874	116,285
ch2_sar_ncxl_20191016t063036242_d_fp_gds	16-10-2019	0.482886, 9.593359	12.650652, 19.986164	25.999045	87.909772, 9.329852	116,561
ch2_sar_nrxl_20191017t115825864_d_fp_d18	17-10-2019	0.583398, 9.593359	10.8, 19.986164	26.000811	87.506973, −14.519421	116,072
ch2_sar_nrxl_20191017t234531221_d_fp_d18	17-10-2019	0.570474, 9.593359	11.475, 19.986164	25.998569	87.483649, −22.178085	112,471
ch2_sar_nrxl_20191019t011733461_d_fp_d18	19-10-2019	0.556473, 9.593359	11.475, 19.986164	25.998984	87.586037, −34.181945	109,500
ch2_sar_ncxl_20191021t061949649_d_fp_gds	21-10-2019	0.523482, 9.593359	11.473073, 19.986164	25.999791	87.621437, −63.365228	102,459
ch2_sar_nrxl_20191022t213646453_d_fp_d18	22-10-2019	0.531336, 9.593359	12.15, 19.986164	25.999746	87.860159, −80.426619	104,200
ch2_sar_ncxl_20191023t210330686_d_fp_d18	23-10-2019	0.486599, 9.593359	12.801045, 19.986164	26.001395	88.123578, −81.162548	94,832
ch2_sar_ncxl_20191024t163255084_d_fp_d18	24-10-2019	0.490309, 9.593359	12.795208, 19.986164	26.000375	88.169761, −85.376036	95,678
ch2_sar_ncxl_20191026t113849791_d_fp_m65	26-10-2019	0.503275, 9.593359	12.825, 19.986164	26.000499	87.572494, −100.383422	98,194
ch2_sar_ncxl_20191027t111245662_d_fp_g26	27-10-2019	0.509141, 9.593359	12.130965, 19.986164	26.001314	87.902608, −120.013863	99,380
ch2_sar_ncxl_20191029t042657221_d_fp_d18	29-10-2019	0.491038, 9.593359	12.796586, 19.986164	26.004718	88.040534, −149.108000	95,485
ch2_sar_nrxl_20191101t105916773_d_fp_d18	1/11/2019	0.530194, 9.593359	12.15, 19.986164	26.003334	87.747836, 145.764459	104,008
ch2_sar_ncxl_20191102t043950913_d_fp_d18	2/11/2019	0.535972, 9.593359	12.15, 19.986164	26.002499	87.911710, 136.798127	105,240
ch2_sar_ncxl_20191103t120442214_d_fp_d18	3/11/2019	0.557860, 9.593359	11.475, 19.986164	26.001475	87.851856, 115.726776	109,978
ch2_sar_ncxl_20191103t175805919_d_fp_mad	3/11/2019	0.564027, 9.593359	11.475, 19.986164	26.001832	87.843557, 113.025163	111,405
ch2_sar_ncxl_20191104t113812494_d_fp_d18	4/11/2019	0.571224, 9.593359	10.774084, 19.986164	26.001926	87.795187, 103.223744	113,027
ch2_sar_ncxl_20191105t150651511_d_fp_d18	5/11/2019	0.555221, 9.593359	11.475, 19.986164	26.00228	87.66181, 101.740069	109,495
ch2_sar_nrxl_20191106t144032517_d_fp_d18	6/11/2019	0.541162, 9.593359	12.15, 19.986164	26.002042	87.942643, 98.568529	106,446
ch2_sar_nrxl_20191107t161214271_d_fp_d18	7/11/2019	0.540642, 9.593359	12.15, 19.986164	26.002902	88.130627, 89.910400	106,331
ch2_sar_ncxl_20191108t095230000_d_fp_d18	8/11/2019	0.551101, 9.593359	11.475, 19.986164	25.991862	88.006451, 82.219519	108,535
ch2_sar_ncxl_20191108t154556810_d_fp_d18	8/11/2019	0.553176, 9.593359	11.475, 19.986164	26.002017	88.008182, 79.774392	108,992
ch2_sar_ncxl_20191108t213931684_d_fp_m65	8/11/2019	0.552081, 9.593359	11.475, 19.986164	26.000272	88.209455, 74.248754	108,860
ch2_sar_ncxl_20191109t211314716_d_fp_mad	9/11/2019	0.546414, 9.593359	12.15, 19.986164	26.000353	88.122131, 64.201509	107,514
ch2_sar_nrxl_20191109t151947658_d_fp_d18	9/11/2019	0.547993, 9.593359	12.15, 19.986164	26.002091	88.161332, 67.066511	107,827
ch2_sar_ncxl_20191111t122919492_d_fp_d18	11/11/2019	0.566197, 9.593359	11.475, 19.986164	26.002133	87.805069, 34.423731	111,695
ch2_sar_ncxl_20191112t215211667_d_fp_d18	12/11/2019	0.560947, 9.593359	10.787579, 19.986164	26.000625	87.867583, 4.599795	110,663
ch2_sar_ncxl_20191112t100519040_d_fp_gds	12/11/2019	0.556343, 9.593359	11.475, 19.986164	26.001229	87.868613, 17.874104	109,567
ch2_sar_ncxl_20191113t212534045_d_fp_d18	13-11-2019	0.553257, 9.593359	11.475, 19.986164	25.999351	87.425005, −11.574374	108,860
ch2_sar_nrxl_20191115t104333906_d_fp_d18	15-11-2019	0.524934, 9.593359	12.15, 19.986164	26.004897	87.710308, −33.925365	102,898
ch2_sar_nrxl_20191115t223022448_d_fp_d18	15-11-2019	0.522318, 9.593359	12.15, 19.986164	26.000199	87.9378, −43.783440	102,291
ch2_sar_ncxl_20191116t220423370_d_fp_d18	16-11-2019	0.509064, 9.593359	12.130173, 19.986164	26.000195	88.319717, −70.051244	99,458
ch2_sar_ncxl_20191117t035728803_d_fp_m65	17-11-2019	0.502798, 9.593359	12.140465, 19.986164	26.000793	87.581983, −55.026475	97,923
ch2_sar_ncxl_20200309t172100282_d_fp_d18	9/3/2020	0.548561, 9.593359	21.615409, 19.986164	26.001482	89.144226, −126.879954	107,235
ch2_sar_ncxl_20200310t225605388_d_fp_d18	10/3/2020	0.538573, 9.593359	22.912646, 19.986164	26.000736	89.237406, −134.147540	105,145
ch2_sar_ncxl_20200311t183930803_d_fp_d18	11/3/2020	0.544870, 9.593359	22.896085, 19.986164	26.000366	89.14718, −143.073214	106,484
ch2_sar_ncxl_20200312t003431195_d_fp_d18	12/3/2020	0.544264, 9.593359	22.89576, 19.986164	26.000919	89.062678, −145.092282	106,496
ch2_sar_ncxl_20200313t235435381_d_fp_d18	13-03-2020	0.535031, 9.593359	22.92549, 19.986164	25.997164	88.730591, −175.902524	104,094
ch2_sar_ncxl_20200313t001429993_d_fp_d18	13-03-2020	0.520629, 9.593359	22.959883, 19.986164	26.000005	88.989595, −160.779604	101,330

ch2_sar_ncxl_20200314t233439044_d_fp_d18	14-03-2020	0.532377, 9.593359	22.932062, 19.986164	25.998766	88.424408, 163.398760	103,571
ch2_sar_ncxl_20200315t231331198_d_fp_d18	15-03-2020	0.538747, 9.593359	22.904088, 19.986164	25.999341	85.780869, −176.521152	105,826
ch2_sar_ncxl_20200315t112336308_d_fp_d18	15-03-2020	0.529707, 9.593359	22.938364, 19.986164	25.999276	85.828915, −168.475885	103,067
ch2_sar_ncxl_20200319t001122747_d_fp_d18	19-03-2020	0.482872, 9.593359	25.299803, 19.986164	26.01496	85.547378, 139.487960	116,727
ch2_sar_ncxl_20200319t060621723_d_fp_d18	19-03-2020	0.487927, 9.593359	25.279744, 19.986164	26.003241	85.57046, 135.608213	118,176
ch2_sar_ncxl_20200320t034747289_d_fp_d18	20-03-2020	0.492372, 9.593359	23.996433, 19.986164	26.009248	85.569284, 125.511457	119,676
ch2_sar_ncxl_20200320t233054415_d_fp_d18	20-03-2020	0.483738, 9.593359	25.291887, 19.986164	25.993962	85.632902, 117.546217	117,312
ch2_sar_ncxl_20200322t050550808_d_fp_d18	22-03-2020	0.574256, 9.593359	21.54512, 19.986164	25.992853	85.861848, 107.943805	113,235
ch2_sar_ncxl_20200325t115928013_d_fp_d18	25-03-2020	0.579556, 9.593359	21.534654, 19.986164	25.998649	85.804669, 68.665651	114,096
ch2_sar_ncxl_20200327t111927967_d_fp_d18	27-03-2020	0.483920, 9.593359	25.296178, 19.986164	25.996564	85.599572, 35.930259	116,909
ch2_sar_ncxl_20200506t164747745_d_fp_d18	6/5/2020	0.580273, 9.593359	21.859055, 19.986164	26.000597	85.508625, −126.396589	86,641
ch2_sar_ncxl_20200508t175741536_d_fp_d18	8/5/2020	0.599591, 9.593359	20.543328, 19.986164	26.004913	86.180788, −161.558742	89,295
ch2_sar_ncxl_20200515t051643228_d_fp_d18	15-05-2020	0.515775, 9.593359	24.245017, 19.986164	25.983093	85.836503, 115.649989	100,630
ch2_sar_ncxl_20200517t003228873_d_fp_d18	17-05-2020	0.515350, 9.593359	24.248865, 19.986164	25.994041	86.305775, 97.355907	100,307

Appendix B. Algorithm: Implemented algorithm to retrieve dielectric constant.

Input: Polarimetric Channels and incidence angle file.
Output: Real part of Dielectric constant.

Simulating the training data by using Eqs. (19) - (26). Simulated data is split into training and testing datasets. Feeding the simulated training dataset to Multilayer Perceptron (MLP) Neural Network.
Back-propagation algorithm (Hayklin, 1994):
Forward Computation:

- Let us represent the training dataset in the epoch as [x(n), d(n)], where the input vector x(n) is fed to the input layer of computation nodes and the desired response vector d(n) is fed to the output layer of computation nodes.

- The activation potentials and function signals of a network are derived by proceeding through layers one by one. The net internal activity level $v_j^{(l)}(n)$ for neuron j in layer l is

$$v_j^{(l)}(n) = \sum_{i=0}^{p} w_{ji}^{(l)}(n) y_j^{(l-1)}(n)$$

where, $w^{(l)}$ = synaptic weight vector of a neuron in layer l.

For i = 0;

$y_0^{(l-1)}(n) = -1$ and $w_{j0}^{(l)}(n) = \theta_j^{(l)}(n)$, where, $\theta_j^{(l)}(n)$ is the threshold applied to neuron j in layer l.

- Let the function (output) signal of neuron j in layer l is:

$$y_j^{(l)}(n) = \frac{1}{1 + \exp(-v_j^{(l)}(n))}$$

- If neuron j is in the first hidden layer (i.e., l = 1);

$y_j^{(0)}(n) = x_j(n)$

where, $x_j(n)$ is the jth element of the input vector x(n).

- If neuron j is in the output layer (i.e., l = L);

$y_j^{(L)}(n) = o_j(n)$

- Computing the error signal

$e_j(n) = d_j(n) - o_j(n)$

where, $d_j(n)$ is the jth element of the desired response vector d(n).

Backward Computation:
- By going backward, layer by layer, computing the δ's (local gradients) of the network:

$$\delta_j^{(L)}(n) = e_j^{(L)}(n)o_j(n)[1 - o_j(n)] \text{ for neuron j in output}$$
layer L.

$$\delta_j^{(l)}(n) = y_j^{(l)}(n)[1 - y_j^{(l)}(n)]\sum_k \delta_k^{(l+1)}(n)w_{kj}^{(l+1)}(n) \text{ for neu-}$$
ron j in hidden layer l.

- Adjusting the weights,

$$w_{ji}^{(l)}(n + 1) = w_{ji}^{(l)}(n) + \alpha\left[w_{ji}^{(l)}(n) - w_{ji}^{(l)}(n - 1)\right]$$
$$+ \eta\delta_j^{(l)}(n)y_j^{(l-1)}(n)$$

where η is the learning-rate parameter and α is the momentum constant.

- Iterating the computation (epochs) until the average square error computed over the entire training set is at a minimum or acceptably small value.

    Testing data is used to validate the regression results. Once the model is fitted and the error is optimized. The model can be used to predict new data.

References

Arnold, J.R., 1979. Ice in the lunar polar regions. J. Geophys. Res. Solid Earth 84 (B10), 5659–5668. https://doi.org/10.1029/JB084iB10p05659.

Babu, A., Kumar, S., Agrawal, S., 2022. Polarimetric Calibration and Spatio-Temporal Polarimetric Distortion Analysis of UAVSAR PolSAR Data. Earth Sp. Sci. 9(4), e2020EA001629:1-16. https://doi.org/10.1029/2020EA001629.

Bhandari, N., Srivastava, N., 2014. Active moon: evidences from Chandrayaan-1 and the proposed Indian missions. Geosci. Lett. 1 (11), 1–12. https://doi.org/10.1186/s40562-014-0011-y.

Bhanu Prakash, M.E., Kumar, S., 2021a. Multifrequency Analysis of PolInSAR-based Decomposition Using Cosine-Squared Distribution. IETE Tech. Rev. Advance online publication. https://doi.org/10.1080/02564602.2021.1892542.

Bhanu Prakash, M.E., Kumar, S., 2021b. PolInSAR decorrelation-based decomposition modelling of spaceborne multifrequency SAR data. Int. J. Remote Sens. 42 (4), 1398–1419. https://doi.org/10.1080/01431161.2020.1829155.

Bhattacharya, A., Porwal, A., Dhingra, S., De, S., Venkataraman, G., 2015. Remote estimation of dielectric permittivity of lunar surface regolith using compact polarimetric synthetic aperture radar data. Adv. Sp. Res. 56 (11), 2439–2448. https://doi.org/10.1016/j.asr.2015.10.007.

Bhiravarasu, S.S., Chakraborty, T., Putrevu, D., Pandey, D.K., Das, A. K., Ramanujam, V.M., Mehra, R., Parasher, P., Agrawal, K.M., Gupta, S., Seth, G.S., Shukla, A., Pandya, N.Y., Trivedi, S., Misra, A., Jyoti, R., Kumar, R., 2021. Chandrayaan-2 Dual-frequency Synthetic Aperture Radar (DFSAR): Performance Characterization and Initial Results 134:1–21. Planet. Sci. J. 2 (4). https://doi.org/10.3847/psj/abfdbf.

Calla, O.P.N., Mathur, S., Gadri, K.L., 2016. Quantification of Water Ice in the Hermite-A Crater of the Lunar North Pole. IEEE Geosci. Remote Sens. Lett. 13 (7), 926–930. https://doi.org/10.1109/LGRS.2016.2554282.

Calla, O.P.N., Mathur, S., Jangid, M., 2014a. Analysis of Dielectric constant & density of Apollo 17 samples. Int. J. Remote Sens. Geosci. 3 (5), 18–22.

Calla, O.P.N., Mathur, S., Jangid, M., 2014b. Study of equatorial regions of Moon with the help of backscattering coefficient obtained from LRO data. J. Earth Syst. Sci. 123 (2), 433–443. https://doi.org/10.1007/s12040-014-0407-2.

Calla, O.P.N., Mathur, S., Jangid, M., Gadri, K.L., 2015. Circular Polarization Characteristics of South Polar Lunar Craters using Chandrayaan-1 Mini-SAR and LRO Mini-RF. Earth. Moon. Planets 115, 83–100. https://doi.org/10.1007/s11038-015-9469-7.

Campbell, B.A., Grant, J.A., Maxwell, T., 2002. Radar Penetration in Mars Analog Environments, in: 33rd Annual Lunar and Planetary Science Conference. Lunar and Planetary Science Conference. Lunar and Planetary Institute, Houston, Houston, Texas, p. 1616:1-2.

Cannon, K.M., Deutsch, A.N., Head, J.W., Britt, D.T., 2020. Stratigraphy of Ice and Ejecta Deposits at the Lunar Poles e2020GL088920:1–11. Geophys. Res. Lett. 47 (21). https://doi.org/10.1029/2020GL088920.

Crawford, I.A., 2015. Lunar resources: A review. Prog. Phys. Geogr. Earth Environ. 39 (2), 137–167. https://doi.org/10.1177/0309133314567585.

Eke, V.R., Bartram, S.A., Lane, D.A., Smith, D., Teodoro, L.F.A., 2014. Lunar polar craters – Icy, rough or just sloping? Icarus 241, 66–78. https://doi.org/10.1016/j.icarus.2014.06.021.

Fa, W., Cai, Y., 2013. Circular polarization ratio characteristics of impact craters from Mini-RF observations and implications for ice detection at the polar regions of the Moon. J. Geophys. Res. E: Planets 118 (8), 1582–1608. https://doi.org/10.1002/jgre.20110.

Fa, W., Wieczorek, M.A., Heggy, E., 2011. Modeling polarimetric radar scattering from the lunar surface: Study on the effect of physical properties of the regolith layer E03005:1–33. J. Geophys. Res. Planets 116 (E3). https://doi.org/10.1029/2010JE003649.

Feldman, W.C., Lawrence, D.J., Elphic, R.C., Barraclough, B.L., Maurice, S., Genetay, I., Binder, A.B., 2000. Polar hydrogen deposits on the Moon. J. Geophys. Res. Planets 105 (E2), 4175–4195. https://doi.org/10.1029/1999JE001129.

Feldman, W.C., Maurice, S., Lawrence, D.J., Little, R.C., Lawson, S.L., Gasnault, O., Wiens, R.C., Barraclough, B.L., Elphic, R.C., Prettyman, T.H., Steinberg, J.T., Binder, A.B., 2001. Evidence for water ice near the lunar poles. J. Geophys. Res. Planets 106 (E10), 23231–23251. https://doi.org/10.1029/2000JE001444.

Fisher, E.A., Lucey, P.G., Lemelin, M., Greenhagen, B.T., Siegler, M.A., Mazarico, E., Aharonson, O., Williams, J.-P., Hayne, P.O., Neumann, G.A., Paige, D.A., Smith, D.E., Zuber, M.T., 2017. Evidence for surface water ice in the lunar polar regions using reflectance measurements from the Lunar Orbiter Laser Altimeter and temperature measurements from the Diviner Lunar Radiometer Experiment. Icarus 292, 74–85. https://doi.org/10.1016/j.icarus.2017.03.023.

Garg, R., Kumar, A., Prateek, M., Pandey, K., Kumar, S., 2022. Land cover classification of spaceborne multifrequency SAR and optical multispectral data using machine learning. Adv. Sp. Res. 69 (4), 1726–1742. https://doi.org/10.1016/j.asr.2021.06.028.

Gold, T., Bilson, E., Baron, R.L., 1976. Electrical properties of Apollo 17 rock and soil samples and a summary of the electrical properties of lunar material at 450 MHz frequency. In: 7th Lunar Science Conference. Pergamon Press Inc, New York, pp. 2593–2603.

Hayklin, S., 1994. Multilayer Perceptrons. In: Neural Networks: A Comprehensive Foundation. Prentice Hall, New Jersey, pp. 138–235.

Hayne, P.O., Aharonson, O., Schörghofer, N., 2021. Micro cold traps on the Moon. Nat. Astron 5, 169–175. https://doi.org/10.1038/s41550-020-1198-9.

Herwartz, D., Pack, A., Friedrichs, B., Bischoff, A., 2014. Identification of the giant impactor Theia in lunar rocks. Science 344 (6188), 1146–1150. https://doi.org/10.1126/science.1251117.

Honniball, C.I., Lucey, P.G., Li, S., Shenoy, S., Orlando, T.M., Hibbitts, C.A., Hurley, D.M., Farrell, W.M., 2021. Molecular water detected on the sunlit Moon by SOFIA. Nat. Astron 5, 121–127. https://doi.org/10.1038/s41550-020-01222-x.

Kausika, B.B., 2013. Polarimetric modeling of lunar surface for scattering information retrieval using Mini-SAR data of Chandrayaan-1. Faculty of Geo-information Science and Earth Observation, University of Twente.

Kumar, S., Babu, A., Agrawal, S., Asopa, U., Shukla, S., Maiti, A., 2022a. Polarimetric Calibration of Spaceborne and Airborne Multifrequency SAR Data for Scattering-Based Characterization of Manmade and Natural Features. Adv. Sp. Res. 69 (4), 1684–1714. https://doi.org/10.1016/j.asr.2021.02.023.

Kumar, S., Garg, R.D., Govil, H., Kushwaha, S.P.S., 2019. PolSAR-Decomposition-Based Extended Water Cloud Modeling for Forest Aboveground Biomass Estimation 2287. Remote Sens. 11 (19), 1–27. https://doi.org/10.3390/rs11192287.

Kumar, S., Govil, H., Srivastava, P.K., Thakur, P.K., Kushwaha, S.P.S., 2020. Spaceborne Multifrequency PolInSAR-Based Inversion Modelling for Forest Height Retrieval 4042:1–27. Remote Sens. 12 (24). https://doi.org/10.3390/rs12244042.

Kumar, S., Singh, A., Sharma, A., Chaudhary, V., Joshi, A., Agrawal, S., Chauhan, P., 2022a. Polarimetric analysis of L-band DFSAR data of Chandrayaan-2 mission for ice detection in permanently shadowed regions (PSRs) of lunar South polar craters. Adv. Sp. Res. Advance online publication. https://doi.org/10.1016/j.asr.2022.01.038.

Landau, E., 2020. Earth and Moon Once Shared a Magnetic Shield, Protecting Their Atmospheres [WWW Document]. URL https://www.nasa.gov/feature/earth-and-moon-once-shared-a-magnetic-shield-protecting-their-atmospheres (accessed 10.30.21).

Li, S., Lucey, P.G., Milliken, R.E., Hayne, P.O., Fisher, E., Williams, J.-P., Hurley, D.M., Elphic, R.C., 2018. Direct evidence of surface exposed water ice in the lunar polar regions. Proc. Natl. Acad. Sci. 115 (36), 8907–8912. https://doi.org/10.1073/pnas.1802345115.

Maiti, A., Kumar, S., Tolpekin, V., Agarwal, S., 2021. A Computationally Efficient Hybrid Framework for Polarimetric Calibration of Quad-Pol SAR Data e2020EA001447:1–22. Earth Sp. Sci. 8 (3). https://doi.org/10.1029/2020EA001447.

Meng, Z., Chen, S., Osei, E.M., Wang, Z., Cui, T., 2010. Research on water ice content in Cabeus crater using the data from the microwave radiometer onboard Chang'e-1 satellite. Sci. China Physics. Mech. Astron. 53, 2172–2178. https://doi.org/10.1007/s11433-010-4159-y.

Mohan, S., Das, A., Chakraborty, M., 2011. Studies of polarimetric properties of lunar surface using Mini-SAR data. Curr. Sci. 101 (2), 159–164.

Mohan, S., Saran, S., Das, A., 2013. Scattering mechanism-based algorithm for improved mapping of water-ice deposits in the lunar polar regions. Curr. Sci. 105 (11), 1579–1587.

Nozette, S., Spudis, P.D., Robinson, M.S., Bussey, D.B.J., Lichtenberg, C., Bonner, R., 2001. Integration of lunar polar remote-sensing data sets: Evidence for ice at the lunar south pole. J. Geophys. Res. E: Planets 106 (E10), 23253–23266. https://doi.org/10.1029/2000JE001417.

Olhoeft, G.R., Strangway, D.W., 1975. Dielectric properties of the first 100 meters of the Moon. Earth Planet. Sci. Lett. 24 (3), 394–404. https://doi.org/10.1016/0012-821X(75)90146-6.

Paige, D.A., Siegler, M.A., Zhang, J.A., Hayne, P.O., Foote, E.J., Bennett, K.A., Vasavada, A.R., Greenhagen, B.T., Schofield, J.T., McCleese, D.J., Foote, M.C., DeJong, E., Bills, B.G., Hartford, W., Murray, B.C., Allen, C.C., Snook, K., Soderblom, L.A., Calcutt, S., Taylor, F.W., Bowles, N.E., Bandfield, J.L., Elphic, R., Ghent, R., Glotch, T.D., Wyatt, M.B., Lucey, P.G., 2010. Diviner Lunar Radiometer Observations of Cold Traps in the Moon's South Polar Region. Science 330 (6003), 479–482. https://doi.org/10.1126/science.1187726.

Patterson, G.W., Bhiravarasu, S.S., Carter, L.M., Cahill, J.T.S., Chakraborty, T., Das, A., Heggy, E., Kumar, R., Morgan, G.A., Neish, C.D., Nypaver, C.A., Palmer, E.M., Pandey, D.K., Plescia, J.B., Putrevu, D., Stickle, A.M., Taylor, P.A., Thomson, B.J., Mini-Rf and DFSAR Teams, 2020. Characterizing the Scattering Properties of the Moon with the LRO Mini-RF and Chandrayaan-2 DFSAR Radars, in: 51st Annual Lunar and Planetary Science Conference,

Lunar and Planetary Science Conference. Lunar and Planetary Institute, Houston, Woodlands, Texas, pp. 2507:1–2.

Putrevu, D., Trivedi, S., Das, A., Pandey, D., Mehrotra, P., Garg, S.K., Reddy, V., Gangele, S., Patel, H., Sharma, D., Sijwali, R., Pandya, N., Shukla, A., Seth, G., Ramanujam, V.M., Kumar, R., 2020. L-and S-band polarimetric synthetic aperture radar on Chandrayaan-2 mission. Curr. Sci. 118 (2), 226–233. https://doi.org/10.18520/cs/v118/i2/226-233.

Ramya, M.N.S., Kumar, S., 2021. PolInSAR Coherence-based Decomposition Modeling for scattering characterization: a case study in Uttarakhand. India. Sci. Remote Sens. 3 (100020), 1–10. https://doi.org/10.1016/j.srs.2021.100020.

Raney, R.K., 2007. Hybrid-Polarity SAR Architecture. IEEE Trans. Geosci. Remote Sens. 45(11), 3397–3404. https://doi.org/10.1109/TGRS.2007.895883.

Raney, R.K., 2006. Dual-polarized SAR and stokes parameters. IEEE Geosci. Remote Sens. Lett. 3 (3), 317–319. https://doi.org/10.1109/LGRS.2006.871746.

Raney, R.K., Brisco, B., Dabboor, M., Mahdianpari, M., 2021. RADARSAT Constellation Mission's Operational Polarimetric Modes: A User-Driven Radar Architecture. Can. J. Remote Sens. 47 (1), 1–16. https://doi.org/10.1080/07038992.2021.1907566.

Raney, R.K., Cahill, J.T.S., Patterson, G.W., Bussey, D.B.J., 2012. The m-chi decomposition of hybrid dual-polarimetric radar data with application to lunar craters E00H21:1–8. J. Geophys. Res. Planets 117 (E12). https://doi.org/10.1029/2011JE003986.

Reid, M., 2011. PDS Data Product Software Interface Specification (SIS) For Mini-RF Advanced Technologies – Forerunner (Mini-SAR) Payload Operations Center. St. Louis.

Rubanenko, L., Venkatraman, J., Paige, D.A., 2019. Thick ice deposits in shallow simple craters on the Moon and Mercury. Nat. Geosci. 12, 597–601. https://doi.org/10.1038/s41561-019-0405-8.

Shafai, S.S., Kumar, S., 2020. PolInSAR Coherence and Entropy-Based Hybrid Decomposition Model. Earth Sp. Sci. 7 (10). https://doi.org/10.1029/2020ea001279, e2020EA001279: 1-17.

Shahsavarhaghighi, S., Sahebi, M.R., Valdanzoej, M.J., Haddadi, G.A., 2013. A Comparison of IEM and SPM Model for Oil Spill Detection Using Inversion Technique and Radar Data. J. Indian Soc. Remote Sens. 41 (2), 425–431. https://doi.org/10.1007/s12524-012-0217-4.

Shukla, S., 2019. Spectroscopy and Bistatic Miniature Radar Lunar Regolith Characterization for Solar Wind Implanted Helium-3 using M3 Spectroscopy and Bistatic Miniature Radar. Faculty of Geo-information Science and Earth Observation, University of Twente.

Shukla, S., Kumar, S., 2018. Hybrid Polarimetric Decomposition Modelling of Lunar Surface for Scattering Characterization using Miniature RADAR data. In: EUSAR 2018; 12th European Conference on Synthetic Aperture Radar. IEEE, Aachen, Germany, pp. 1–6.

Shukla, S., Kumar, S., Tolpekin, V.A., 2019. Petrophysical Insights Into Lunar Mafic Extrusive Basalts Over Reiner Gamma Formation. IEEE J. Sel. Top. Appl. Earth Obs. Remote Sens. Advance online publication. https://doi.org/10.1109/jstars.2019.2909352.

Shukla, S., Tolpekin, V., Kumar, S., Stein, A., 2020. Investigating the retention of solar wind implanted helium-3 on the moon from the analysis of multi-wavelength remote sensing data 3350:1–24. Remote Sens. 12 (2). https://doi.org/10.3390/rs12203350.

Spudis, P.D., Bussey, D.B.J., Baloga, S.M., Cahill, J.T.S., Glaze, L.S., Patterson, G.W., Raney, R.K., Thompson, T.W., Thomson, B.J., Ustinov, E.A., 2013. Evidence for water ice on the Moon: Results for anomalous polar craters from the LRO Mini-RF imaging radar. J. Geophys. Res. Planets 118 (10), 2016–2029. https://doi.org/10.1002/jgre.20156.

Spudis, P.D., Bussey, D.B.J., Butler, B., Carter, L., Gillis-Davis, J., Goswami, J., Heggy, E., Kirk, R., Misra, T., Nozette, S., Robinson, M.S., Raney, R.K., Thomson, B., Ustinov, E., 2009. The Mini-SAR Imaging Radar on the Chandrayaan-1 Mission to the Moon, in: 40th Annual Lunar and Planetary Science Conference, Lunar and Planetary Science Conference. Lunar and Planetary Institute, Houston, Woodlands, Texas, pp. 1098:1–2.

Tavares, F., 2018. Ice Confirmed at the Moon's Poles [WWW Document]. URL https://www.nasa.gov/feature/ames/ice-confirmed-at-the-moon-s-poles (accessed 11.11.21).

Thomson, B.J., Bussey, D.B.J., Neish, C.D., Cahill, J.T.S., Heggy, E., Kirk, R.L., Patterson, G.W., Raney, R.K., Spudis, P.D., Thompson, T.W., Ustinov, E.A., 2012. An upper limit for ice in Shackleton crater as revealed by LRO Mini-RF orbital radar L14201: 1-4. Geophys. Res. Lett. 39 (14). https://doi.org/10.1029/2012GL052119.

Tomar, K.S., 2015. Hybrid polarimetric decomposition for aboveground biomass estimation using semi-empirical modelling. Faculty of Geo-information Science and Earth Observation, University of Twente.

Tomar, K.S., Kumar, S., Tolpekin, V.A., 2019. Evaluation of Hybrid Polarimetric Decomposition Techniques for Forest Biomass Estimation. IEEE J. Sel. Top. Appl. Earth Obs. Remote Sens. 12 (10), 3712–3718. https://doi.org/10.1109/JSTARS.2019.2947088.

Vasavada, A.R., Paige, D.A., Wood, S.E., 1999. Near-Surface Temperatures on Mercury and the Moon and the Stability of Polar Ice Deposits. Icarus 141 (2), 179–193. https://doi.org/10.1006/icar.1999.6175.

Vashishtha, A., Kumar, S., 2021. Characterization of geomorphological features of lunar surface using Chandrayaan-1 Mini-SAR and LRO Mini-RF data. Quat. Int. 575–576, 338–357. https://doi.org/10.1016/j.quaint.2020.08.018.

Verma, S., Kumar, S., Mishra, V.N., Raj, R., 2022. Multifrequency Spaceborne Synthetic Aperture Radar Data for Backscatter-Based Characterization of Land Use and Land Cover. Front. Earth Sci. 10 (825255), 1–24. https://doi.org/10.3389/feart.2022.825255.

Vondrak, R., Keller, J., Chin, G., Garvin, J., 2010. Lunar Reconnaissance Orbiter (LRO): Observations for Lunar Exploration and Science. Space Sci. Rev. 150, 7–22. https://doi.org/10.1007/s11214-010-9631-5.

Williams, J.-P., Greenhagen, B.T., Paige, D.A., Schorghofer, N., Sefton-Nash, E., Hayne, P.O., Lucey, P.G., Siegler, M.A., Aye, K.M., 2019. Seasonal Polar Temperatures on the Moon. J. Geophys. Res. Planets 124 (10), 2505–2521. https://doi.org/10.1029/2019JE006028.

Wolfe, E.W., Bailey, N.G., Lucchitta, B.K., Muehlberger, W.R., Scott, D. H., Sutton, R.L., Wilshire, H.G., 1981. The Geologic investigation of the Taurus-Littrow valley, Apollo 17 landing site, USGS Professional Paper 1080. Washington. https://doi.org/10.3133/pp1080.

Woodhouse, I.H., 2006. Introduction to Microwave Remote Sensing, 1st ed. CRC Press, Taylor & Francis Group, Boca Raton. https://doi.org/10.1201/9781315272573.